Fabrication and Optical Properties of Upconverting Nanoparticle/ Graphene Hybrids

by

Fathi Souissi

Thesis submitted to the University of Ottawa
In partial fulfillment of the requirements for the degree of

Master's in Physics

Department of Physics
Faculty of Science
University of Ottawa

Abstract

Over the past decade, graphene/nanomaterial hybrids have gained a great interest in various applications due to their unique optical properties. This work explores lanthanide doped upconverting nanoparticles (UCNPs)/graphene hybrid nanomaterials. Here, core/shell structures comprising β-$NaGdF_4$:Yb^{3+}(20%),Er^{3+}(2%)@$NaGdF_4$ and α-$NaGdF_4$:Yb^{3+}(20%), Er^{3+}(2%)@$NaGdF_4$ with oleate as capping agent were synthesized and characterized. The choice of lanthanide ions (Yb^{3+} and Er^{3+}) and their concentrations plays an important role to make these nanoparticles undergo two optical processes (upcoversion and downshifting) capable to convert near-infrared excitation to visible and near-infrared emission. In order to make hybrid systems, these nanoparticles were combined with graphene films. The morphology and the optical behavior of the hybrid samples were studied by microscope and hyperspectral imaging. The multi-energy sublevels from the 4f electronic configuration of lanthanides, their long excited state lifetime and the high carrier mobility of the graphene expected to open an exciting possibility of interaction, however, UCNPs/Graphene hybrid nanomaterial exhibits a minimal response when subjected to 980 nm laser illumination.

Dedicated to

My father's soul

My loving wife Nesrine

My princess Ameerah

Acknowledgments

First, I would like to thank my two co-supervisors, Professor Adina Luican-Mayer and Professor Eva Hemmer for giving me the opportunity to work with their groups. I am grateful to your wisdom and support while guiding me towards research avenues. I really appreciate your passion and your efforts towards helping me to finish my thesis.

I would also like to thank Dr. Emille M. Rodrigues for her help, support, and training during the past years. I want to extend my thanks to my colleagues Nan Lui who ran all TEM measurements and Samantha Scarfe for her training in the graphene transfer.

I am thankful to all the group members including post-docs, student and honour students and I have the pleasure to work with them.

I want to address a very especial thanks to all my teachers for giving me a jump start in the world of knowledge. I want to dedicate this work to my father's soul, and I won't forget that I have done my thesis during COVID-19 pandemic.

I like to thank my wife for her love, understanding, encouragement and help throughout my MSc degree.

Finally, I am eternally grateful for the guidance and support provided by my family members throughout my studies.

Table of Contents

List of Tables

List of Figures

List of Abbreviations

2D	Two-dimensional
AFM	Atomic Force Microscopy
CVD	Chemical Vapour Deposition
CRET	Cross-Relaxation Energy Transfer
CUC	Cooperative Upconversion
DI	Deionized
EC	Electronic Configuration
EMU	Energy Migration Upconversion
ESA	Excited State Absorption
ETU	Energy Transfer Upconversion
GO	Graphene Oxide
HSI	Hyperspectral Imaging
IR	Infrared
NIR	Near-Infrared
NPs	Nanoparticles
PAA	Poly(acrylic acid)

PA	Photon Avalanche
PDMS	Poly(dimethylsiloxane)
PL	Photoluminescence
REE	Rare Earth Elements
UC	Upconversion
UCNPs	Upconverting Nanoparticles
TEM	Transmission Electron Microscopy
XRD	X-Ray Diffraction
FWHM	Full Width at Half Maximum

Chapter I

Introduction

It is well known that most of the light reaching the earth from the sun is infrared (IR) in nature and it is a great source of energy. Since the discovery of IR light many technological innovations have been developed. Lanthanide-based upconverting nanoparticles (UCNPs) are a type of nanomaterials that can convert low-energy photons (e.g., IR light) into high-energy photons (e.g., visible light) through a process called upconversion [1–5]. Graphene is a two-dimensional (2D) carbon material that has unique electronic and mechanical properties, making it attractive for a wide range of applications [6, 7]. By combining UCNPs with graphene, the resulting hybrid material can owe these advantages and provide an excellent approach for various applications in optoelectronics, bio-imaging and sensing [7–11]. Here in this work, the goal is to use UCNPs as photoabsorber and the graphene as an efficient charge transporter to generate a photocurrent. Subsequently, in the following literature, an extensive overview on lanthanides is highlighted besides graphene properties.

I.1 Introduction to Lanthanides

Lanthanide chemistry started in 1787 when C. A. Arrhenius found a black mineral in the Swedish village of Ytterby. He called this element oxide yttria or earth yttria [1, 2]. In 1794, Johan Gadolin succeeded to identify this oxide as gadolinite [1, 2, 12]. Soon afterwards in 1803, M. H. Klaproth, J. J. Berzelius and W. Hisinger discovered another

earth named ceria. Later around 1839-1843, this compound was resolved into oxide of cerium and lanthanum by the Swede C.G. Mosander [2]. It took more than a century until Henry Moseley proved that there were 15 elements that share certain characteristics with lanthanum, hence the collective term of "lanthanides" [2]. More specifically, lanthanides (Ln) are a group of 15 consecutive chemical elements with atomic number from 57 to 71. Lanthanides referred to the category of rare earth elements (REE) including Yttrium (Y) and Scandium (Sc). They are also known as f-block elements since the 4f sub-shell is getting filled progressively as the atomic number changes from 57 to 71.

I.1.1 Electronic Configuration of Lanthanides

The lanthanides have a general electronic configuration (EC) given by $[Xe]4f^{1-14}5d^{0-1}6s^2$, where [Xe] is the EC of the nearest noble gas Xenon [2, 13, 14]. At Lanthanum (La), the 5d sub-shell is lower in energy than 4f, so Lanthanum has the EC $[Xe]4f^05d^16s^2$. As the atomic number increases, the 4f orbitals contract and become more stable than 5d so that Cerium has the electron configuration $[Xe]4f^15d^16s^2$. This trend continues with Praseodymium (Pr) having the arrangement $[Xe]4f^36s^2$, then pursue for the elements Neodymium (Nd) to Europium (Eu), all of which have configuration $[Xe]4f^{4-7}6s^2$. After Europium, the next electron is added to the 5d orbital due to the presence of half-filled sub-shell, thus Gadolinium (Gd) being $[Xe]4f^75d^16s^2$. The earlier pattern is resumed at Terbium (Tb) to have the configuration $[Xe]4f^96s^2$ and, succeeding elements to Ytterbium (Yb) being $[Xe]f^{10-14}6s^2$. For the last lanthanide, Lutetium (Lu, Z = 71), the added electron entered to the 5d orbital due to the fully filled of 4f sub-shell, so that Lu has $[Xe]4f^{14}5d^16s^2$ arrangement. In forming ions, lanthanides are like the case of the transition metals, electrons are moved first from 6s and 5d orbitals before they are taken from 4f, so that all Ln^{3+} ions have $[Xe]4f^n$ arrangement as shown in Table I.1 [13, 15]. The presence of f sub-shell has a great influence on the oxidation state exhibited by these elements and their properties.

Table I.1: Electronic configuration of lanthanides and their common ions [15].

Atom	Electronic structure	Ln^{3+}	Ln^{4+}	Ln^{2+}
La	$[Xe]4f^{0}5d^{1}6s^{2}$	$[Xe]4f^{0}$		
Ce	$[Xe]4f^{1}5d^{1}6s^{2}$	$[Xe]4f^{1}$	[Xe]	
Pr	$[Xe]4f^{3}6s^{2}$	$[Xe]4f^{2}$	$[Xe]4f^{1}$	
Nd	$[Xe]4f^{4}6s^{2}$	$[Xe]4f^{3}$	$[Xe]4f^{2}$	$[Xe]4f^{4}$
Pm	$[Xe]4f^{5}6s^{2}$	$[Xe]4f^{4}$		
Sm	$[Xe]4f^{6}6s^{2}$	$[Xe]4f^{5}$		$[Xe]4f^{6}$
Eu	$[Xe]4f^{7}6s^{2}$	$[Xe]4f^{6}$		$[Xe]4f^{7}$
Gd	$[Xe]4f^{7}5d^{1}6s^{2}$	$[Xe]4f^{7}$		
Tb	$[Xe]4f^{9}6s^{2}$	$[Xe]4f^{8}$	$[Xe]4f^{7}$	
Dy	$[Xe]4f^{10}6s^{2}$	$[Xe]4f^{9}$	$[Xe]4f^{8}$	$[Xe]4f^{10}$
Ho	$[Xe]4f^{11}6s^{2}$	$[Xe]4f^{10}$		
Er	$[Xe]4f^{12}6s^{2}$	$[Xe]4f^{11}$		
Tm	$[Xe]4f^{13}6s^{2}$	$[Xe]4f^{12}$		$[Xe]4f^{13}$
Yb	$[Xe]4f^{14}6s^{2}$	$[Xe]4f^{13}$		$[Xe]4f^{14}$
Lu	$[Xe]4f^{14}5d^{1}6s^{2}$	$[Xe]4f^{14}$		

I.1.2 Oxidation State of Lanthanides

All lanthanide elements show an oxidation state of +3. However, among the list, some of them (Samarium, Europium, and Ytterbium) exist in their +2-oxidation state. For instance, Europium (atomic number 63) has the electronic configuration $[Xe]4f^{7}6s^{2}$, it loses two electrons from 6s energy level and becomes highly stable in half-filled configuration $4f^{7}$. Hence, it forms Eu^{2+} ions, then changes to the common oxidation states of lanthanides +3 and forms Eu^{3+}, acting as a strong reducing agent. Ytterbium (atomic number 70) has a fully filled f-orbital in the Yb^{2+} state, it has the same behavior as Europium for being a strong reducing agent after reverting to Yb^{3+}. A few elements in the lanthanide series (Cerium, Praseodymium, Neodymium, Terbium and Dysprosium) exhibit +4-oxidation state due to the high stability of an empty (Ce^{4+}), half-filled (Tb^{4+}) 4f orbital. The +4-oxidation state of Cerium is preferred as it achieves a noble gas configuration [Xe], but, it

returns to +3-oxidation state and then acting as a strong oxidant. Trivalent lanthanide ions (Ln^{3+}) are the most common and stable oxidation state.

I.1.3 Energy Levels of Lanthanides

Thanks to their electronic structure, Ln^{3+} have common optical properties. They possess specific emission colours related to each Ln^{3+} ion and they have discrete energy levels [16–18]. The emission bands of lanthanide ions originate from f→f transitions. Typically, the luminescent emission of Ln ions occurs from the lowest level of the higher miltiplet (populated by non-radiative cascade decay from the excited upper level) to the ground state. The Dieke diagram in Figure I.1 shows the energy levels of the most limenescent used lanthanide ions [19–23].

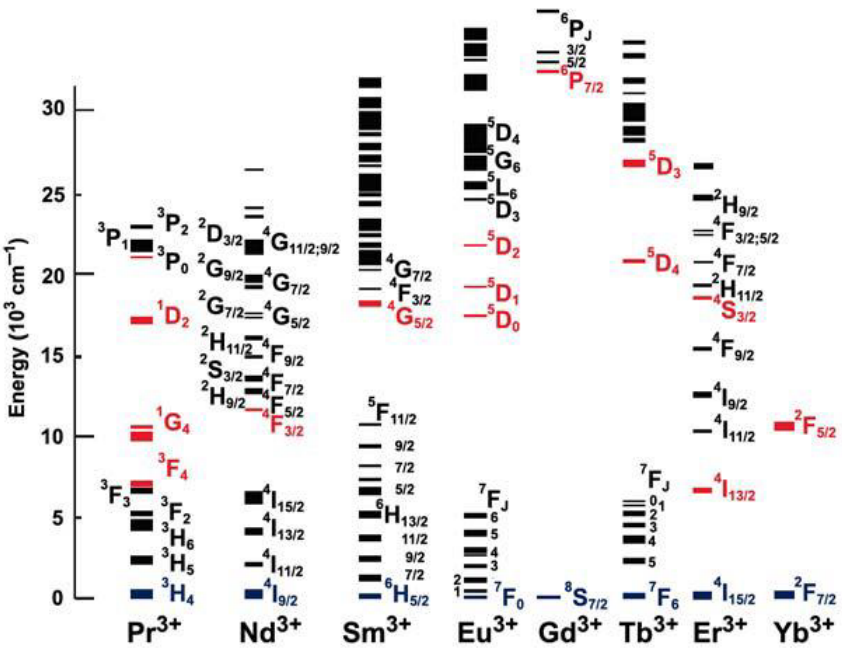

Figure I.1: Dieke diagram of the energy levels of some trivalent lanthanide ions. The main luminescent levels are drawn in red, while the fundamental level is indicated in blue. Taken from [22].

The 4f-electrons are shielded by filled 5s and 5p orbitals. Consequently, they are weakly affected or perturbed by the surrounding environment effects and ligands. As a result of

this isolation, the crystal-field effects are very weak compared to the Coulomb interactions between the electrons and spin orbital coupling. This interaction has the largest contribution to the energy level splitting [2, 17, 21]. Each level from the 4f configuration of free lanthanide ions can be expressed with the term $^{2S+1}L_J$, where S is the total spin quantum number, L is the total orbital quantum number and J is the total angular momentum quantum number. According to Hund's rule, the ground term for the free ion is determined by the highest values of L and S quantum numbers while the spin-orbit coupling quantum number, J, ranges from $L - S \leq J \leq L + S$ and takes, for the fundamental level, the value $J = L - S$ for $n < 7$ (La-Eu) and $J = L + S$ for $n \geq 7$ (Gd-Lu).

I.1.4 Lanthanide Luminescence and Selection Relues

The luminescence of Ln^{3+} ions originating from electronic transitions between 4f levels could be either electric dipole or magnetic dipole, or even quadrupole in character. Generally, the electric dipole transitions are strongly forbidden based on the Laporte quantum mechanical selection rules (Laporte's rule: $\Delta l = \pm 1$), while the magnetic dipole transitions are allowed but unlikely and therefore have an intrinsic low intensity. Moreover, these electronic transitions can occur through the intermixing of higher EC with f-states by local crystal field effect or vibronic coupling. The rule can be relaxed for Ln^{3+} ions embedded in a suitable medium leading to unique optical properties such as a sharp emission band, reliable photostability and long excited-state lifetime [4, 24–26]. These features make lanthanide-doped upconverting materials ideal candidates for a variety of applications.

I.2 Lanthanide-based Upconverting Nanoparticles

Lanthanide-doped upconversion materials usually consist of a suitable inorganic and photostable host embedded with various trivalent lanthanide ions [3, 27–29].

I.2.1 Energy Transfer Mechanism of Upconversion (UC)

The UC process has been extensively studied, and there are multiple mechanisms behind this phenomenon: excited state absorption (ESA), energy transfer upconversion (ETU), cooperative upconversion (CUC), photon avalanche (PA) and energy migration upconversion (EMU), as described in Figure I.2 [3, 27]..

I.2.2 Excited State Absorption (ESA)

ESA is a UC type that requires a continuous absorption of multiple low energy photons by a single Ln^{3+} ion called activator. As illustrated in Figure I.2 **a)** the equidistant ladder-like structure of the 4f sub-shell facilitates photons of a specific energy to excite ions from the ground state G to the first excited state E_1. If the excited state ion at energy level E_1 absorbs a second photon before it relaxes back to the ground state, it is boosted to the higher-lying excited state E_2. Then, a radiative decay from E_2 results in an upconverted emission of photons with an energy greater than the energy of photons being absorbed [5, 30, 31]. The ESA takes place only if the intermediary excited state E_1 is sufficiently long-lived and the photon flux high enough so that the second photon is being absorbed prior the relaxation of state E_1 back to the ground state G.

I.2.3 Energy Transfer Upconversion (ETU)

ETU is often considered to be the main mechanism responsible for the observed upconversion in Ln-based materials. Unlike the ESA, ETU process requires two or more neighboring lanthanide ions to generate the upconversion. Figure I.2 **b)** presents the mechanism responsible for this type of UC photoluminescence. In this process, one ion is known as the sensitizer; this ion is initially excited to level E_1 through absorption of a photon with energy equivalent to the transition from G to E_1. Then, the absorbed energy is transferred to a ground state ion 2 near the sensitizer ion promoting it to the intermediate excited state E1. This second ion is referred as the activator. Upon transfer of energy, the sensitizer ion returns down to its original ground state becoming available for another

photon absorption event. The energy from this second photon is then pumped into the already excited activator ion residing in the E_1 energy level resulting in a promotion to a higher energy level, E_2. Subsequently, radiative relaxation from the E_2 energy level results in UC photoluminescence by the activator ion [5, 30]. The upconversion efficiency of the ETU process is highly dependent on the distance between the activator and sensitizer, the similar ladder-like arrangement of energy levels amongst the participating entities, and the long-lived nature of these electronic transitions.

I.2.4 Cooperative Upconversion (CUC)

The CUC process involves three ions, of which ion 1 and ion 2 should be typically the same type (sensitizer). In Figure I.2 **c)**, ion 1 and ion 2 are first excited to level E_1 followed by the subsequent and simultaneous transfer of all energy to ion 3, which is thereby excited to a higher state E_2. The excited ion 3 relaxes to the ground state, emitting upconverted light. The efficiency of CUC is generally lower than that of the ESA or ETU processes [5].

I.2.5 Photon Avalanche (PA)

PA is a less common mechanism that produces UC as presented in Figure I.2 **d)**. The PA mechanism is based on cross-relaxation energy transfer (CRET) between closely spaced ions in a material. Initially all ions are in state G and at some point, one of the ions will be promoted to state E_1 by weak, non-resonant, ground state absorption and then promoted to an upper level E_3 via ESA. After the metastable-level population is established, cross-relaxation energy transfer occurs between the excited ion and a neighboring ground-state ion, resulting in both ions occupying the intermediate level E_1. These two ions can then undergo ESA to populate state E_3, thereby producing strong UC emission as an avalanche process [5, 30, 32, 33].

I.2.6 Energy Migration Upconversion (EMU)

EMU is a UC process type that based on energy transfer within core/shell architectures. Figure I.2 **e)** illustrates lanthanide ions that are involving in an EMU process. The lanthanide ions designed for producing this process are classified into four types: the sensitizer (type I), the accumulators (type II), the migrators (type III), and the activators (type IV) [4, 23, 34]. The EMU process starts with the absorption of a low energy photon by the sensitizer populating its first excited state E_1. Then, the energy is subsequently transferred to an adjacent accumulator ion promoting it to an excited state E_1. Through successive energy transfers from the sensitizer, the accumulator collects enough energy to reach a level in resonance with a migrator. At this stage, the migrator ion extracts the excitation energy from high-lying energy states of the accumulator, followed by random energy hopping through the migrator ion sublattice. Finally, the energy is trapped by an activator, giving out UC emissions form of radiative relaxation at a shorter wavelength than what was initially absorbed by the sensitizer ions. To regulate energy exchange interaction between the accumulator and the activator, the sensitizer/accumulator and the activator are spatially confined in different layers of a core/shell structure, which is essential for eliminating deleterious cross relaxation.

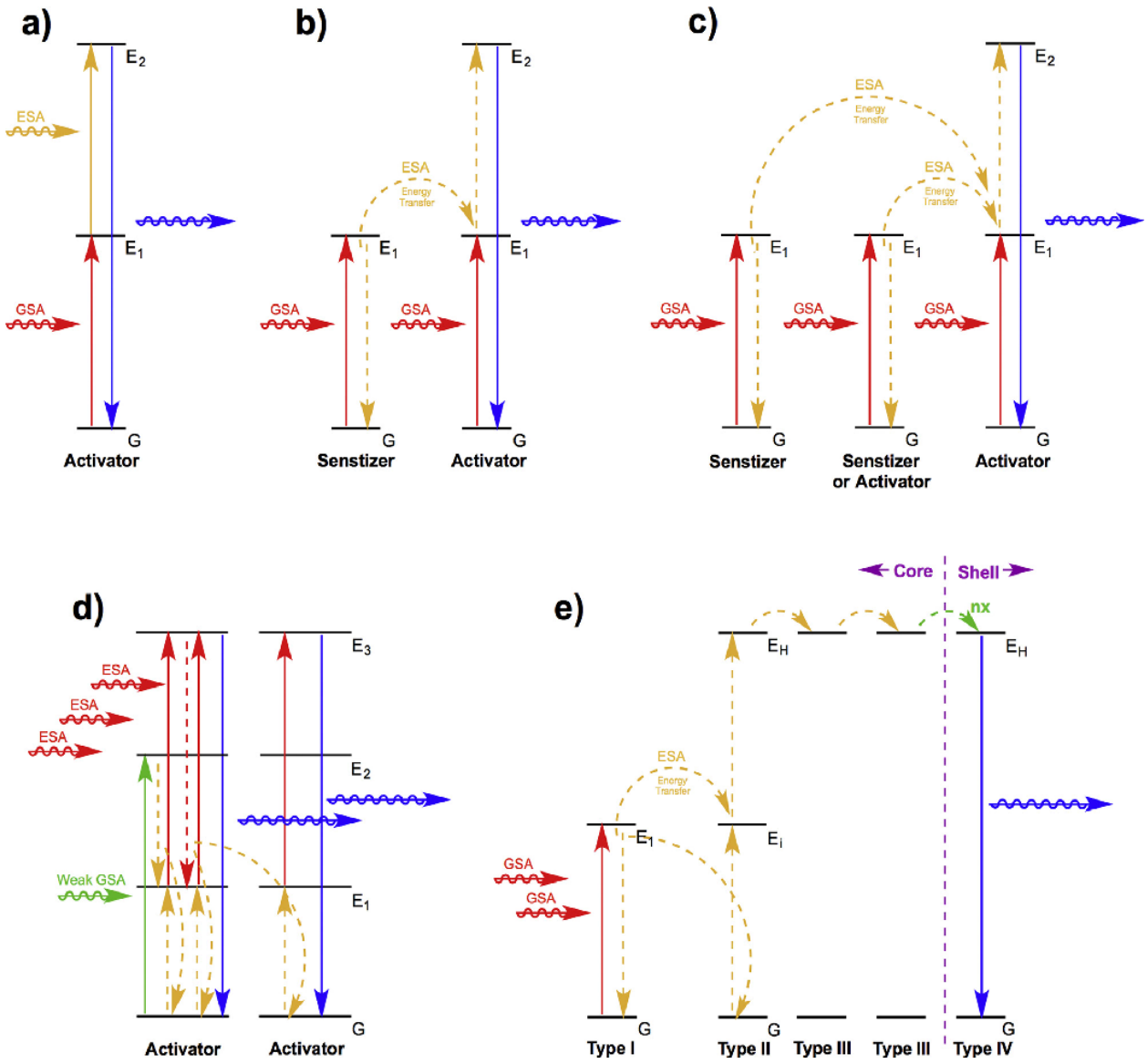

Figure I.2: Energy level diagrams of a) excited state absorption upconversion, b) energy transfer upconversion, c) cooperative upconversion, d) photon avalanche, and e) energy migration upconversion. E_i (i=1,2,3) represents an excited state, GSA represents ground state absorption. Solid and wavy red arrows refer to ground state photon absorption events, solid and wavy blue arrows indicate UC emissions, solid yellow arrows refer to ESA, dashed yellow arrows represent ETU and relaxation pathways via ESA. Line colors are not related to any wavelength. Reprinted from [27].

I.3 Upconverting Nanoparticle Composition

Generally, upconverting nanoparticles (UCNPs) are composed of two components: an inorganic host matrix and doping ions called sensitizer and activators (emission centers) [30, 35–37].

I.3.1 Host Lattice Choice

A typical host lattice should have low phonon energy and low cristal field symmetry to minimize the non-radiative energy losses and maximize radiative emission. Many host materials have been selected for Ln-based NPs, such as lanthanide sesquioxide (Ln_2O_3), trifluoride (LnF_3), sodium tetrafluoride ($NaLnF_4$), phosphate ($LnPO_4$), yttrium aluminum oxide garnet (YAl_5O_{12}), vanadate ($LnVO_4$), and oxysulfide (Ln_2O_2S) [38]. $NaGdF_4$ and $NaYF_4$ have been shown to be a good host candidates for UCNPs since they have a great lattice matching with the dopant ions, low phonon energy and high chemical stability [23, 25, 35, 39]. The later two materials can crystallize in two different polymorphs: the hexagonal (β) phase and the cubic (α) phase as shown in Figure I.3 [40].

A crystalline host lattice exhibiting a low phonon energy environment is beneficial to the photon UC process, where the non-radiative decay rate of lanthanides via multiphonon relaxation can effectively be suppressed. The difference between these two crystallized phases comes from the lattice positions assigned to cations. In the hexagonal phase,a lower crystal symmetry (low phonon energy) that could result in more allowed f-f transitions compared to the cubic phase which leads to a higher crystal symmetry and fewer allowed f-f transitions. [40–42]. The crystaline phase is controloble by adjustiong the molar ratio of Ln^{3+} to Na^{+}[41, 43, 44]. Generally, The chemical stability and phase transformation of $NaLnF_4$ NPs are depended on the dopants concentration and synthesis conditions [43].

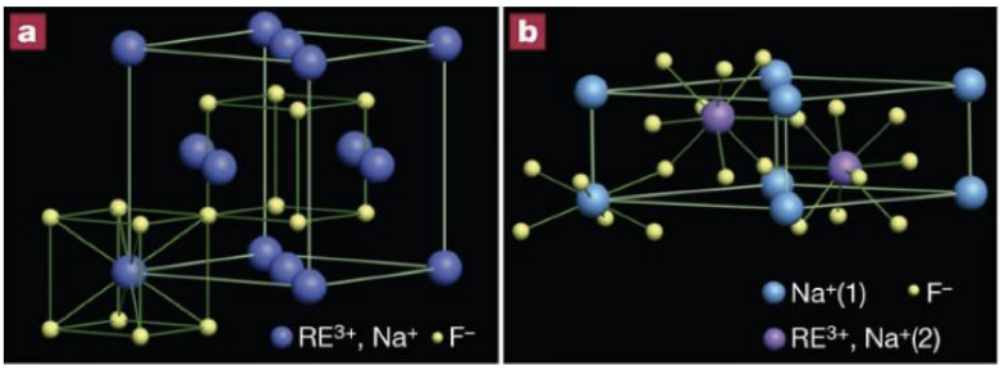

Figure I.3: Schematic of the two crystalline phases of $NaLnF_4$: a) cubic lattice, b) hexagonal lattice. Reprinted from [40].

I.3.2 Sensitizer

The sensitizer is a component that is able to transfer the captured energy to activators present within the host lattice of the UCNPs. A good sensitizer has a large absorption cross-section in the range of the desired excitation energy. For these reasons, the lanthanide ion Yb^{3+} is considered the best sensitizer because of its unique energy level structure with only one long-lived excited state which has a relatively low energy gap.
This makes Yb^{3+} particularly sensitive to the energy of the incoming photons, and allows it to absorb light even at low intensities.[27, 45, 46]. Yb^{3+} ions can efficiently absorb energy from pump sources at shorter wavelengths (around 980 nm) and then transfer this energy to the erbium ions Er^{3+}

I.3.3 Activator

The activator is the ion that emits the upconverted radiation. The major requirements of a good activator are having more than one excited state energy level and long-lived excited states enabling further pumping of multiple photons through energy transfer with sensitizer ions. The selection of activator is based on the desired emission wavelength [27, 45, 46]. Common activator choices are Tm^{3+}, Er^{3+} and Ho^{3+} ions. The choice of activators and sensitizers used in an UCNPs system is dependent on the application for which the nanoparticle is intended. Various UCNPs can be created, one of the most efficient UCNPs

systems consists of Yb^{3+} sensitizer co-doped with either Er^{3+} or Tm^{3+} activators. Usually, the doping level of these ions is around 20% for Yb^{3+}, 2% for Er^{3+}, and 0.5% for Tm^{3+} [46, 47]. A detailed energy level diagram and photoluminescence (PL) spectra of UC system is provided in Figure I.4. The Yb^{3+} ion acts as a sensitizer and Er^{3+} ion as an activator in the upconversion process. Under the 980 nm laser excitation, an electron pumped from the ground state ($^2F_{7/2}$) of Yb^{3+} ion to its excited state, ($^2F_{5/2}$), and subsequently, this energy is transferred from Yb^{3+} ($^2F_{5/2}$) to Er^{3+}($^4I_{11/2}$) energy level. This happens as these levels are closer in energy. A further excitation of electron from Er^{3+} ($^4I_{11/2}$) to the Er^{3+} ($4^F_{7/2}$) occurs via a second energy transfer from Yb^{3+} ($^2F_{5/2}$) level after exciting the ground state of Yb^{3+}. The excited electrons decay first non-radiatively to $^2H_{11/2}$, $S_{3/2}$, and $^4F_{9/2}$ energy levels and then radiatively decay to the ground state $^4I_{15/2}$ of Er^{3+} ion releasing green and red emissions, respectively [44].

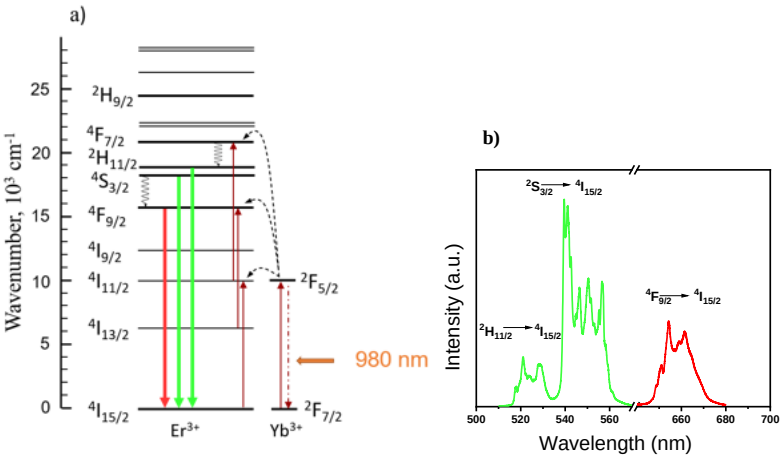

Figure I.4: Energy transfer mechanism, b) emission spectra of the Yb^{3+}/Er^{3+} ion pair via the upconversion processes under NIR (980 nm) excitation.

I.3.4 Upconverting Nanoparticle Core/Shell Concept

The UC emission efficiency of NPs depends on the radiative and non-radiative decays of the excited states of dopant ions. These non-radiative decays are caused by different mechanisms like surface defects and the vibration of capping ligands, which are deleterious to the UC emissions. To overcome this concern, forming core/shell structures is a way to enhance the UC emission efficiency. This architecture protects the dopant ions involved in the UC process via shell that isolates them from the environement effects [23, 27, 37, 48–50]. Usually, the lattice spacing of the core and the shell must be matching or similar to each other in order to minimize the non-radiative relaxation processes at the interface, which increase the UC emission [45]. It has been reported that growing core/shell and core/shell/shell structures has been adopted to maximize the upconversion luminescence [23, 51–53]. Song and coworkers demonstrated that the core/shell structure can significantly increase the luminescence efficiency by improving the NIR photons absorption (active shell) and minimizing the luminescence quenching (outer inert shell). An active shell growth ($NaYF_4$: Yb, Nd) on core UCNPs ($NaYF_4$:Yb,Nd,Tm) enhanced about 2 times the emission intensity, and the subsequent $NaYF_4$ inert shell growth enhanced about 10 times the emission intensity under 980 nm laser excitation. However, these improvements were found more efficient for 808 nm laser excitation where the emission intensity was enhanced about 22 times by the active shell growth and about 20 times more after growing the inert shell [48]. It was noticed that increasing the shell thickness can result in a decrease of the energy transfer efficiency, thus an optimal shell thickness should be estimated [23, 48]. Figure I.5 illustrates a core/shell NP where the shell is inert.

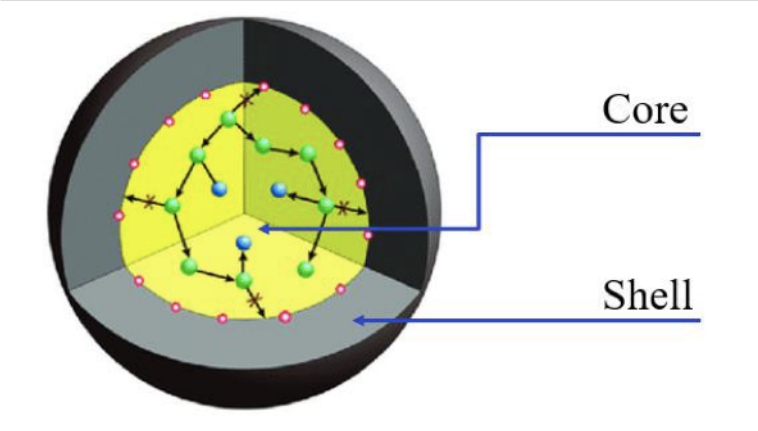

Figure I.5: Core-shell UCNPs: doped core with an inert shell(no absorbing or emitting lanthanide dopant); the colored balls in the core area depict lanthanide dopants; the red circles at the interface represent surface quenching sites; the black arrows indicate random energy transfer pathways. Figure taken from [50].

I.4 Graphene

I.4.1 Introduction to Graphene

Graphene is a single two-dimensional (2D) sheet of sp^2 hybridized carbon atoms that tightly bound in a honeycomb lattice as presented in Figure I.6 (a) [7, 54–57]. The name of graphene comes from graphite, a multilayer graphene structure Figure I.6 (b), which is naturally available from minerals. The first mention of graphite appeared in 1840 by Dr. Schafhaeutl [55]. The work on graphene started in 1947 by Wallace [55, 58]. In 1986, Boehm et al. used the term graphene after an extensive work with reduced graphite [55]. However, the experimental discovery of graphene only happened in 2004 by Novoselov and Geim when they used a scotch tape as a simple technique to extract a flake of graphite with a thickness of just one atom. This discovery was awarded the Nobel Prize in 2010 because it paved the way to the 2D in material sciences [55, 58]. The isolated graphene from bulk of graphite was the first and most studied 2D material.

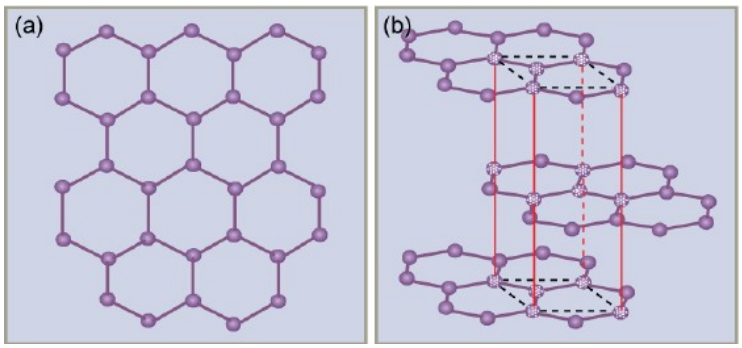

Figure I.6: (a) Graphene is a honeycomb lattice of carbon atoms. (b) Graphite can be viewed as a stack of graphene layers [55]. Taken from [59]

.

I.4.2 Graphene Synthesis Methods

Since the first study of graphene, several techniques were established for its synthesis. The most used methods are briefly described below.

Mechanical exfoliation: This method was used for the first synthesis of graphene which consists of peeling-off graphite layers using scotch tape, and transferring it to an appropriate substrate, such as a SiO_2 wafer [55, 60].

Chemical vapor deposition (CVD): This technique was discovered in 2009, a monolayer of graphene was synthesized on metal like copper or nickel by catalytic decomposition at high temperature of carbonated gases, such as methane or ethylene [55, 61, 62].

Epitaxial graphene on SiC: This method was used first by Forbeau et al. in 1998 to prepare ultrathin films of graphene by heating silicon carbide under vacuum [55, 63].

Liquid phase exfoliation of graphite: This process is very simple and cheap. A graphene sheets can be obtained by dispersing graphite in a specific solvent generally not aqueous such as N-methyl-pyrrolidone or pure hydrazine [55, 64].

This method leads to a low quality of graphene due to some factors such as the agregation or oxidation that can happed during the process.

Reduction of graphene oxide: This method consists of reducing oxygen content from graphene oxide (GO) through a chemical reduction using a reducing agent such as hydrazine, sodium borohydride, or ascorbic acid, to reduce the functional groups on the

surface of GO or throught a thermal reduction methods by heating GO in an inert atmosphere, such as argon or nitrogen, to high temperatures [6, 55, 65].
These different methods produce graphene with different size (μm^2 to cm^2) and thikness (monolayer, bilayer and multilayer), which rendering it suitable for many applications.

I.4.3 Graphene Properties

Graphene is a one atom thick layer in a planar honeycomb lattice. Due to its sp^2 hybridization, every carbon has three σ bonds and one π bond, which also creates a delocalized π-system being responsible for the good conductivity of graphene. To explain the motion of the delocalized electrons of π bonds a crystallographic description for the graphene lattice is needed.
Naturally, graphene does not correspond to a Bravais lattice. It consists of two trigonal sub-lattices labeled A and B with two-atom basis distancing of 0.142 nm as seen in Figure I.7 [58, 66].

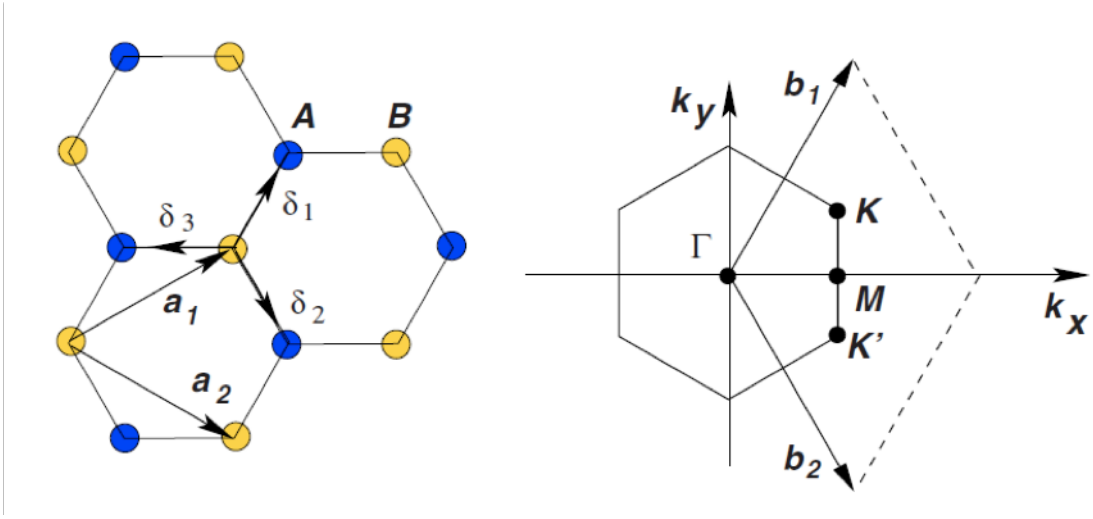

Figure I.7: Honeycomb lattice and its Brillouin zone. Left: lattice structure of graphene, made out of two interpenetrating triangular lattices (a_1 and a_2 are the lattice unit vectors, and δ_i, i=1, 2, 3 are the nearest-neighbor vectors). Right: corresponding Brillouin zone. The Dirac cones are located at the K and K' points. Taken from [58].

The nearest neighbors of A sites are always B sites and vice versa. Conveniently, the lattice vectors can be written as

$$a_1 = \frac{a}{2}(3, \sqrt{3}), \quad a_2 = \frac{a}{2}(3, -\sqrt{3}), \tag{I.1}$$

where $a_1 = 1.42$ Å is the carbon-carbon distance. The reciprocal-lattice vectors are given by

$$b_1 = \frac{2\pi}{3a}(1, \sqrt{3}), \quad b_2 = \frac{2\pi}{3a}(1, -\sqrt{3}). \tag{I.2}$$

The first Brillouin zone is a hexagon, where the two points K and K' at the corners and their position in the momentum space are given

$$K = (\frac{2\pi}{3a}, \frac{2\pi}{3\sqrt{3}a}), \quad K' = (\frac{2\pi}{3a}, -\frac{2\pi}{3\sqrt{3}a}). \tag{I.3}$$

The three nearest neighbor vectors in real space are given by

$$\delta_1 = \frac{a}{2}(1, \sqrt{3}), \quad \delta_2 = \frac{a}{2}(1, -\sqrt{3}), \quad \delta_3 = a(1, 0). \tag{I.4}$$

Thanks to its structural features, graphene is a material with several unique and extraordinary properties. More specifically, graphene behaves as semi-metallic material or zero-bandgap semiconductor where its valance and conductive bands touch in a point called Dirac point as shown in Figure I.8. It has a high electron mobility at ambient conditions 10000 $cm^2V^{-1}S^{-1}$ and it can be easily p or n doped. It is worth mentioning that the mobilities range widely depend on the type of graphene or substrate.

All above properties make graphene the most intensively studied 2D material and to be a prime candidate for a wide range of applications.

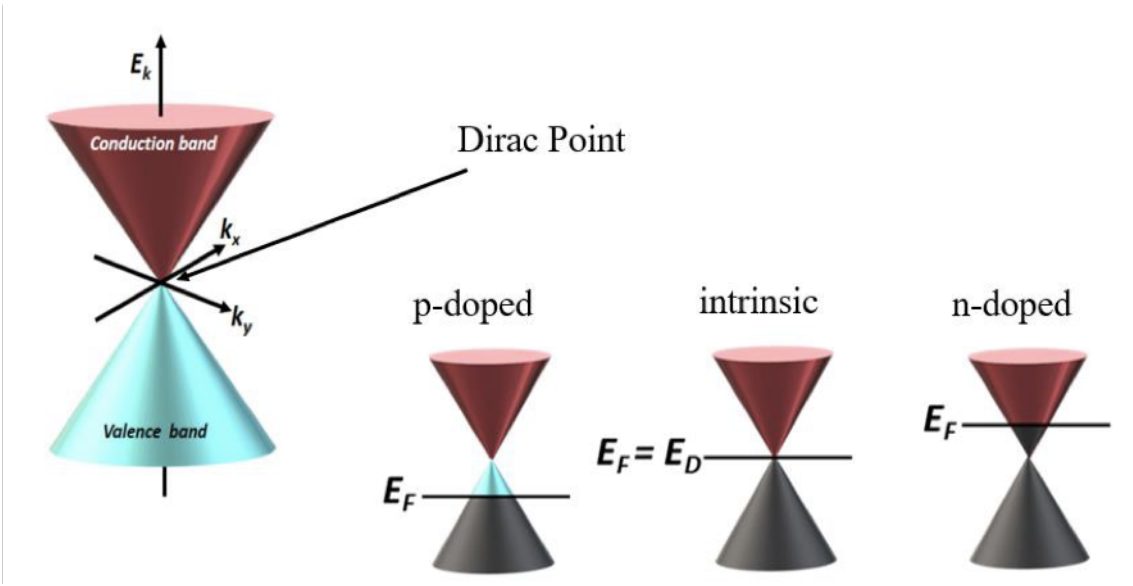

Figure I.8: Schematic band structures of graphene. E_F: Fermi energy, E_D: Dirac electron. Taken from [67].

I.5 Recent Work

Owing to the distinctive photoluminescence properties of lanthanide-based NPs and the fascinating properties of the graphene, there has been a great interest in combining these materials for various applications. Multiple research works studied the current state of the art and the progress over the hybrids of graphene and its derivative combined with different nanomaterials [7–11, 68]. More specifically, some studies reported potential application in NIR photodetectors such as combining UCNPs with a graphene/GaAs heterojunction to enhance the performance of photodetectors by broadening the absorption limitation of GaAs, improving the upconversion luminescence of SiO_2 coated UCNPs combined with graphene, and exhibiting an ultrahigh photoresponsivity by incorporating UCNPs, graphene, and micro-pyramidal poly(dimethylsiloxane) (PDMS) film [8–10]. Moreover, combining TiO_2 with UCNPs and reduced graphene increases TiO_2 photocatalytic activity [68]. Not limited to that, these hybrids have touched the bioapplications. In case of biosensing, graphene/metallic NPs hybrid achieved a better sensitivity and selectivity of biomolecules compared to the standard gold. Also, graphene/NPs hybrids have led to the enhancement of image contrast, cancer therapies, and stem cell differentiation [7, 11].

While these studies have highlighted a significant progress in different hybrid materials, hybrids based on graphene and UCNPs are underrepresented in the literature. Additionally, there is a need for thorough investigation into the fundamental understanding of UCNPs/graphene.

The distinct narrow upcoversion emission, the long lifetime of lanthanide doped UCNPs, and the high carrier mobility of graphene can be combined all together in a hybrid system for enabling some applications such as NIR photodetectors and photothermal nanoheaters. While many characterization techniques such as photocurent mesurement and dynamic photoresponse have been used to study the UCNPs/graphene hybrid materials[9], there is still room for improvement, i.e., using the hyperspectral imaging (HSI) technique to combine spectroscopy and imaging information in order to gain a deeper understanding of the underlying mechanism of UCNPs/graphene.

I.6 Hyperspectral Imaging (HSI)

HSI is a technique that combines both advanced spectroscopy and imaging to attain sufficient spatial and spectral information of an object that could be based on any kind of spectroscopy such as photoluminescence, absorption and scattering [69–73]. From an analyzed sample a three-dimensional set of data (sometimes referred as hypercube data or as an image cube) is generated, where x-y coordinates are the spatial axes and the z is the spectral information providing more detailed spectroscopic informatio of the sample than traditional spectroscopy [71, 74]. Originally, HSI was developed in the field of satelites and food processing [38]. Recently, it has been emerged in nanoscale materials including metal nanoparticles, carbon nanotubes and graphene [75]. This technique can image across a broad spectrum from the visible to the NIR. It is believed that HSI technology is a potential technique for property investigation and manipulation of nanomaterial for various applications.

In the context of this thesis, HSI will be used to thoroughly analyse the emission properties of UCNPs/graphene hybrid system. The fundamental principles of this technique are simplified in Figure I.9.

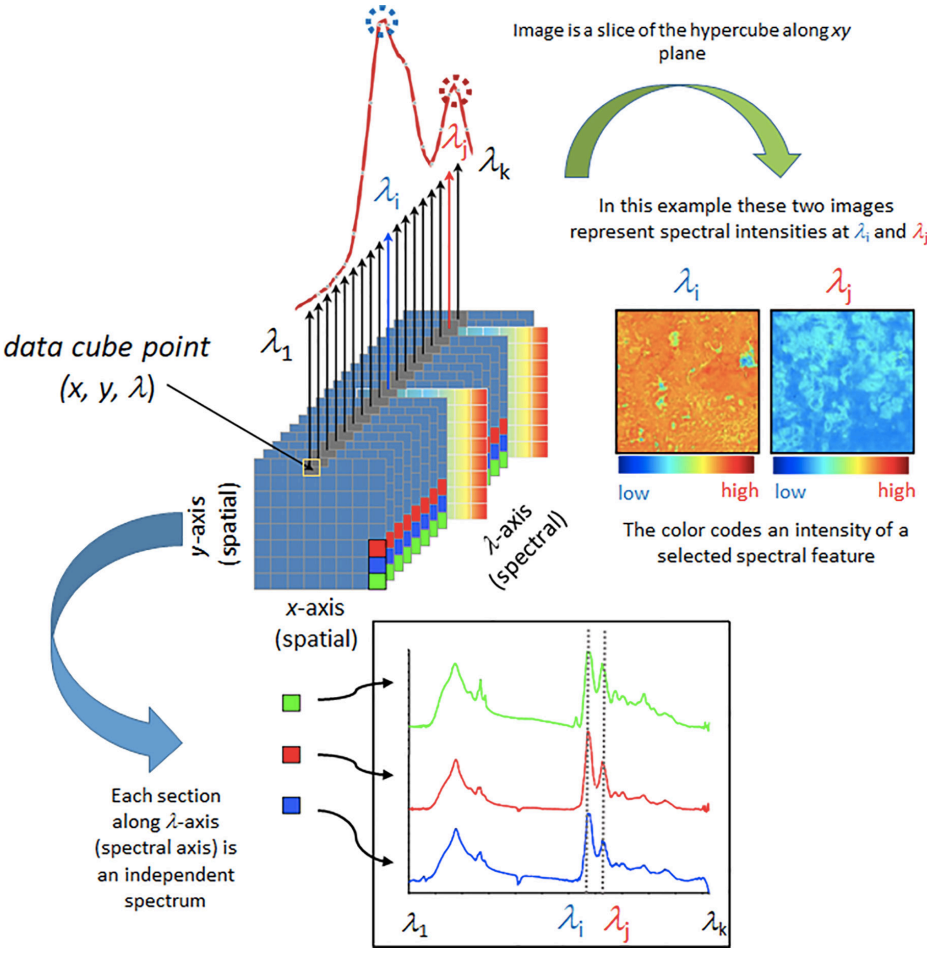

Figure I.9: Simplified scheme presenting fundamental principles of a spectral data hypercube and visualization based on the most straightforward spectral information available, spectral intensity. Reproduced from [76].

I.7 Objectives

As explained before, multiple studies explored the properties of lanthanide-based UCNPs coated with silica (SiO_2) combined with graphene's derivative, or graphene combined with different nanomaterials. Given the absence of literature on the study of UCNPs/graphene hybrids, especially when UCNPs are prepared via microwave-assisted synthesis, this thesis is dedicated to thoroughly investigating and understanding the optical properties of UCNPs/graphene hybrids.

Therefore, the specific objectives of this thesis are stated below.

- Synthesis of core/shell NPs via microwave-assisted synthesis following established protocols.
- Characterizing the synthesized NPs.
- Transferring a graphene film from Cooper foil to glass substrate using a developed approach.
- Preparing the hybrid nanomaterial containing the UCNPs and graphene, then investigating its photoluminescence using HSI technique.

As mentioned earlier, due to the multi-energy sublevels stemming from the 4f electronic configuration of lanthanides, coupled with their extended excited state lifetime and the high carrier mobility of graphene, the hypothesis suggests a potential energy transfer between UCNPs and graphene. The HSI is a technique to study the local PL properties to investigate the emission homogeneity of the hybrid and evaluate any energy transfer.

Chapter II

Experimental Techniques and Sample Preparation

This chapter outlines the experimental methods and characterization techniques common to the subsequent chapters.

II.1 Materials and Reagents

All reagents were used without any purification. Gadolinium oxide (Gd_2O_3, 99.999%), ytterbium oxide (Yb_2O_3, 99.998%), and erbium oxide (Er_2O_3, 99.99%) were purchased from Alfa Aesar. Trifluoroacetic acid (TFA, CF_3COOH, 98%), sodium trifluoroacetate (Na-TFA, CF_3COONa, 98%), 1-octadecene (ODE, $C_{18}H_{36}$, 90%), oleic acid (OA, $C_{18}H_{34}O_2$, 90%), oleylamine (OAm, $C_{18}H_{35}NH_2$, 70%), nitrosonium tetrafluoroborate ($NOBF_4$, 98%), trisodium citrate dihydrate ($C_3H_9Na_3O_9$, 99%), and Copper etchant were purchased from Sigma Aldrich. Toluene (99.8%) was purchased from Fisher Scientific (a global supplier of laboratory equipment). Ethanol (99%), hexane, and acetone were purchased from Commercial Alcohols and Fisher Chemicals. A commercially available graphene grown by CVD on Copper foil was purchased from Graphenea.

II.2 Microwave-assisted Synthesis of Lanthanide-based Nanoparticles ($NaGdF_4$:Yb^{3+}, Er^{3+}@$NaGdF_4$)

The nomenclature of ($NaGdF_4$:Yb^{3+},Er^{3+}@$NaGdF_4$) describes a type of UCNPs known as a core/shell structure where $NaGdF_4$:Yb^{3+},Er^{3+} refers to the core of the NP which is made up of a compound called sodium gadolinium fluoride $NaGdF_4$ doped with Ytterbium Yb^{3+} and Erbium Er^{3+} ions. The term (@ $NaGdF_4$) indicates that there is a shell layer surrounding the core structure. In this case, the shell layer is inert and composed of $NaGdF_4$, the same compound as the core. The synthesis of UCNPs was based on an established protocol that was previously reported in [9, 41, 44, 77, 78].

II.2.1 Lanthanide Trifluoroacetate $Ln(TFA)_3$ as Core Precursor (Ln = Gd^{3+}, Yb^{3+}, and Er^{3+})

To synthesize $NaGdF_4$:Yb^{3+}(20%), Er^{3+}(2%) NPs, 1.25 mmol of [$Ln(TFA)_3$] precursor was prepared by mixing Gd_2O_3 (176.7 mg, 0.488 mmol), Yb_2O_3 (49.3 mg, 0.125 mmol), and Er_2O_3 (4.8 mg, 0.0125 mmol) in 10 mL of 1:1 trifluoroacetic acid-H_2O in a 100 mL three-neck round bottom flask. The mixture was refluxed at 100 °C and stirred at 800 rpm for approximately 5 h, until the solution became clear, followed by overnight drying at 50 °C to evaporate the solvent. The equation for chemical reaction is shown in Figure II.1.

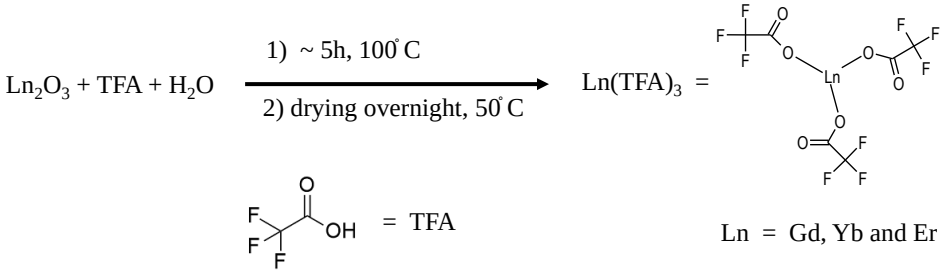

Figure II.1: Reaction scheme for the preparation of [$Ln(TFA)_3$] from Ln_2O_3, Ln = Gd^{3+}, Yb^{3+}, and Er^{3+}.

II.2.2 Lanthanide Trifluoroacetate [$Ln(TFA)_3$] as Shell Precursor ($Ln = Gd^{3+}$)

In brief, for the shell precursor 1.25 mmol of [$Gd(TFA)_3$] was prepared by mixing (1.25 mmol, 226 mg) of Gd_2O_3 and 10 mL mixture of H_2O and TFA with a ratio of 1:1 in a flask under stirring at 100 °C until the solution turned transparent. The first part of the shell precursor takes only 1 hour. After that the solution was dried overnight at 50 °C.

II.2.3 Synthesis of $NaGdF_4$:Yb^{3+}(20%),Er^{3+}(2%): Core UCNPs

To synthesize hexagonal crystal phase β-$NaGdF_4$:Yb^{3+}(20%),Er^{3+}(2%) NPs, 3.75 mmol of Na-TFA (510 mg) was added to a flask containing 1.25 mmol of previously prepared $Ln(TFA)_3$. The ion ratio of Na^+ to Ln^{3+} is 3:1 [44]. A 20 mL mixture of ODE, OAm, and OA in a 2:1:1 volume ratio was added to the mixture, then the solution was subjected to a degassing process under vacuum and stirring at 100 °C for 30 min. A volume of 10 mL from the degassed solution was transferred into a 35 mL microwave vessel tightly sealed after purging with N_2, then placed into a CEM Discover SP microwave reactor.

β-$NaGdF_4$:Yb^{3+}(20%),Er^{3+}(2%) core NPs were grown by subjecting the reaction mixture to the microwave radiation under constant stirring and the following conditions: stirring at room temperature for 1 min, rapid heating up to T_1 = 270 °C, this stage lasts 5 min, holding the reaction for 1 s, then rapid cooling to T_2 = 260 °C, followed by holding the reaction for 10 min. After that, a rapid and gradual cooling to 50 °C was performed over a period of 5 min.

For the cubic crystal phase α-$NaGdF_4$:Yb^{3+}(20%),Er^{3+}(2%) NPs, 1.25 mmol of Na-TFA (170 mg resulting in 1:1 Na^+ to Ln^{3+} ion ratio) and 20 mL of ODE, OAm, and OA in a 2:1:1 volume ratio was added to the three-neck flask containing the prepared $Ln(TFA)_3$. After that, the solution was degassed under the same conditions described before. A volume of 10 mL from this solution was transferred into 35-mL microwave vessel and flushed with N_2. The microwave vessel was tightly sealed and placed into the microwave reactor. The α-$NaGdF_4$:Yb^{3+}(20%),Er^{3+}(2%) NPs, were grown by placing the reaction solution under

the same microwave heating profile, however, T_1 was 300 °C and T_2 was 230 °C.
Following the synthesis, the reaction mixture containing the obtained NPs in hexagonal or cubic phase were transferred to a 50 mL centrifuge tube and a 1:3 volume ratio of hexane-ethanol was added for dilution in order to precipitate the NPs, after shaking with vortex, the mixture was centrifuged at 8000 rpm for 20 min. After discarding the solvent, the precipitated NPs were dispersed in 10 mL of ethanol, and 15 mL of H_2O was added, followed by precipitation under the same centrifugation condition as described above. This step is mandatory to remove any NaF as it is a potential by-product especially when using excess of Na^+. In case of hexagonal phase NPs synthesis, the last washing can be done more than one time. Finally, another dispersion and precipitation in 10 mL of ethanol was required to remove all residue of water before storing the synthesized NPs in 5 mL of hexane for the subsequent shell growth procedure. The excessive washing of NPs can remove the organic ligands that are essential for stabilizing the UCNPs in solution and causes the loss of their dispersion stability. If this case happens, then the dispersibility in hexane or toluene can be restored by adding 0.2 mL of OA to NP dispersion and a stirring overnight at room temperature is required. Figure II.2 illustrates the reaction scheme of NPs growth.

II.2.4 Synthesis of $NaGdF_4$:Yb^{3+}(20%),Er^{3+}(2%)@$NaGdF_4$: Core-shell UCNPs

To grow undoped $NaGdF_4$ shells on hexagonal and cubic phase of core NPs previously synthesized, each stored solution containing core NPs was divided into two equal volumes. One half was kept aside as a reference, and the other half was precipitated and dispersed in 1 mL of ODE. The dispersed NPs were transferred to the three-neck flask containing the dry shell precursor [$Gd(TFA)_3$] after adding 170 mg of Na-TFA with 1:1 ion ratio Na^+ to Gd^{3+} and 20 mL mixture of ODE and OA with 1:1 volume ratio. The solution was degassed at 100 °C for 30 min. A 10 mL from the degassed mixture was transferred into a 35 mL microwave vessel and purged with N_2. After sealing the vessel, it was placed in the microwave reactor under the following conditions: stirring for 1 min at room temperature,

rapid heating up to 250 °C for the hexagonal phase and 230 °C for the cubic phase, then holding the reaction for 10 min and cooling gradually to 50 °C for 5 min. The resulting core-shell NPs were washed and stored using the same protocol used for the core only NPs.

II.3 Surface Modification

The synthesized β-$NaGdF_4$:Yb^{3+}(20%),Er^{3+}(2%)@$NaGdF_4$ were subjected to a surface modification in order to render them water dispersible using procedures reported in previous work [43, 79–83].

II.3.1 Oleate (OA^-) Ligand Removal

Ligand-free NPs (LF-NPs) were prepared through acidic treatment of oleate-capped NPs (OA-NPs) previously synthesised [38, 43]. Into an Erlenmeyer flask, 15 mL of HCl solution (pH = 1.5) were added to 150 mg of OA-NPs dispersed in 15 mL of hexane. The biphasic mixture was stirred overnight at room temperature. Subsequently, the mixture

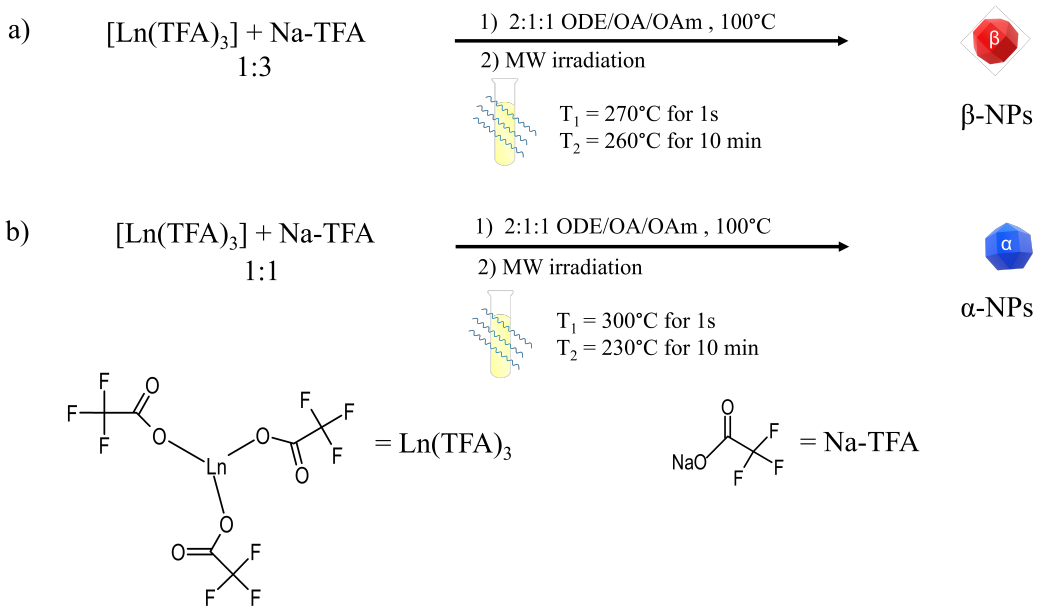

Figure II.2: Reaction scheme for the preparation of a) β-NPs and b) α-NPs through microwave-assisted synthesis. T_1 and T_2 are microwave reaction temperatures. MW refers to microwave

was transferred into a separatory funnel. The aqueous phase containing the NPs was isolated and mixed with 45 mL of acetone, then centrifuged for 20 min at 10000 rpm to precipitate the NPs. The resulting LF-NPs were stored in 5 mL of water or ethanol before characterization.

II.3.2 Citrate-Coated β-$NaGdF_4$ NPs

Citrate-coated NPs were obtained by stirring a mixture of 5 mL of hexane containing about 70 mg of OA-NPs and 5 mL of trisodium citrate buffer (0.2 M, pH = 3) for 3 h at 40 °C [43]. The biphasic mixture was poured into a separatory funnel, the aqueous phase containing the NPs was separated and mixed with 25 mL of acetone to precipitate the NPs. After centrifuging the mixture for 15 min at 10000 rpm, the organic solvent was removed, and the precipitated NPs were re-dispersed in 5 mL of trisodium citrate buffer (pH = 7). The new dispersion was stirred for 2 h, then washed three times using water and acetone for precipitation and subsequent centrifugation at the same condition described before. The obtained citrate-coated NPs were stored in 5 mL of sodium citrate solution (0.02 M).

II.3.3 Polyacrylic Acid (PAA) Surface Modification

To prepare PAA-coated NPs, 100 mg of OA-capped NPs dispersed in 5 mL of chloroform and 120 mg of PAA dispersed in 10 mL of ethanol were mixed and stirred overnight [38]. Subsequently, the NPs were precipitated in acetone with volume ratio (8:1 acetone:NPs dispersion) and centrifuged for 20 min at 10000 rpm. The recovered NPs were dispersed in water and washed two times with 8:1 acetone:water mixture. The resulting PAA-capped NPs were stored in 5 mL of water.

II.4 Graphene Transfer

Graphene transfer is the process of moving a piece of graphene film from a Copper or Nickel surface to another surface of a desired material, such as a glass substrate. In this work, the most common transfer process addressed by several researchers, which involves

the wet etching of the Copper foil and fishing the graphene by the substrate from below, was applied [55, 84–86]. The procedure started by cutting the graphene-copper foil coated PMMA into the desired size (5 mm x 5 mm). Then, the sample was submerged in an acidic Copper etchant solution at 70 °C with the PMMA layer facing upwards until all Copper dissolves. After that, the transparent graphene-PMMA film was transferred to a deionized (DI) water bath using an etchant-resistant spoon. After 5 min, the graphene-PMMA film was transferred to another dish containing fresh DI water. To ensure that all etchant was washed, this process should be repeated at least three times. At this point, the graphene-PMMA flake was fished out of the water bath using a clean glass substrate tilted at a 45°-angle. This step is very challenging to keep a planar structure of the graphene without any fractures or wrinkles. For better adhesion of the graphene and to evaporate any residue of water, the sample was annealed for 15 min at 50 °C at ambient atmosphere, then placed inside the fume-hood environment. The next day, the PMMA layer was dissolved by placing the sample in a bath of acetone for 30 min followed by washing with isopropanol. Finally, the graphene film has been successfully transferred onto a glass substrate.

The graphene transfer procedure is illustrated in Figure II.3.

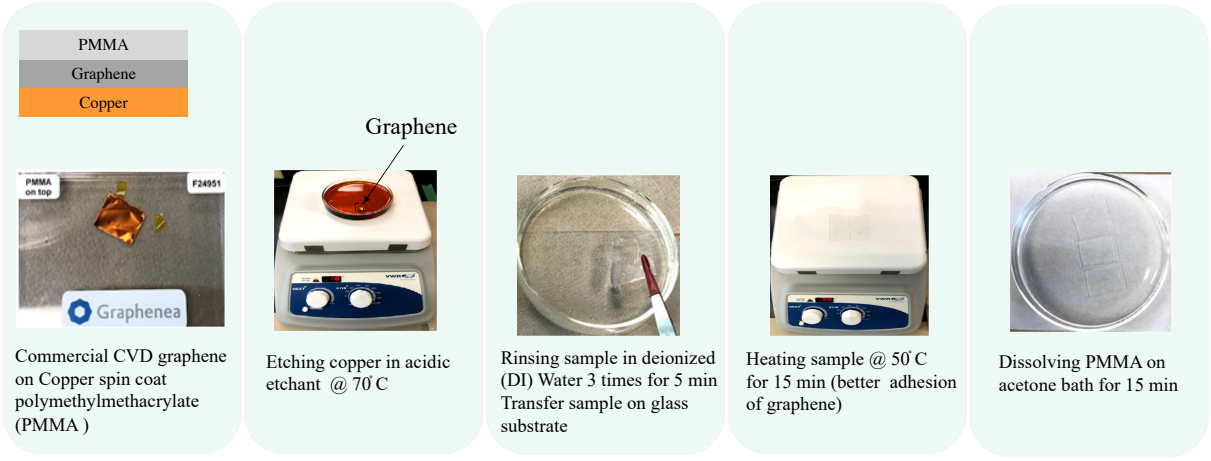

Figure II.3: Illustration of transferring graphene film from copper foil to a glass substrate.

II.5 Combining Lanthanide-based Nanoparticles and Graphene Film

In order to prepare UCNPs/Graphene hybrid samples, two different methods were performed.

II.5.1 Simple Solvent Evaporation

This method involves a drop-casting of dispersed NPs in hexane into the graphene surface using a microliter pipette. The solvent was evaporated at room temperature leaving a heterogeneous film of NPs on top of the graphene and the glass substrate.

II.5.2 Spin Coating Deposition

To prepare a homogeneous film of NPs deposited on graphene, 2 mL of dispersed NPs in hexane were spin-coated at 4000 rmp for 30 s using CY-SPC4 small spin coater as illustrated in Figure II.4.

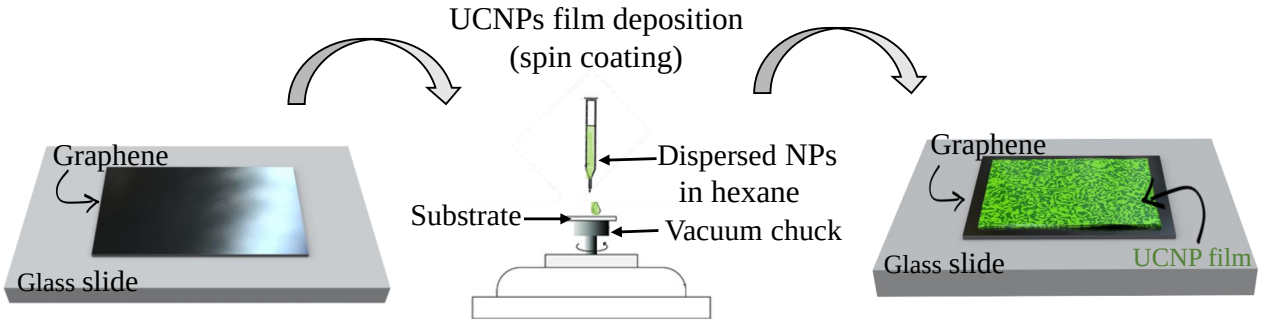

Figure II.4: Schematic diagram of preparing UCNPs/Graphene by spin-coating deposition.

II.6 Characterization Techniques

The different characterization technique used in the present work will be described below.

II.6.1 Powder X-Ray Diffraction

To determine the crystalline phase of the of synthesized NPs, powder X-ray diffraction (XRD) was performed on each sample for identification. Before the measurement, NP dispersions were dropcasted and dried on a glass substrates then, subjected to XRD using a Rigaku Ultima IV Diffractometer (Cu Kα, $\lambda = 1.5401$ Å), operating at 44 kV and 40 mA with scan speed 1°/ min. The XRD patterns were acquired in a range from 20 ° to 60°.

II.6.2 Transmission Electron Microscopy

The morphology and size of the synthesized NPs were obtained by transmission electron microscopy (TEM) using a FEI Tecnai Spirit microscope operated at 120 kV. Samples were prepared on a Formvar/carbon film supported on a 300-mesh Copper TEM grid after dilution. The particle sizes were extracted from the TEM image using the software ImageJ. The average size was calculated by analyzing 200 particles per sample using OriginPro software. The TEM measurements were performed by Ms Nun Liu.

II.6.3 Photoluminescence Spectroscopy

Photoluninescence (PL) measurements were acquired on NP dispersions in hexane using a 1 cm optical cuvette and on dried film of NPs deposited on glass substrates. The spectroscopic analysis was performed using a custom-built hyperspectral microscope (IMA Upconversion^{TM} by PhotonEtc, Montreal, Canada). This optical system contains a Princeton Instruments SP-2360 monochromator/spectrograph, an inverted Nikon Eclipse Ti optical microscope, a set of galvanometer mirrors, visible and NIR emission filters, a Princeton Instruments ProEM EMCCD camera for the visible emission. The instrument is also equipped with a holder for cuvettes to measure PL on dispersions. The excitation source used for this work was a 980 nm laser diode with an approximate power density of 104 mW/cm^2.

II.6.4 Hyperspectral Imaging (HSI)

HIS was performed on UCNPs/graphene hybrid samples and on UCNPs/glass (as a reference) using the instrument described above. The upconverted visible emissions were obtained at room temperature by scanning a selected area (10 μm x 10 μm) of UCNPs/graphene hybrid and UCNPs/glass . The probed emission bands were the green (510-570 nm) and the red (640-680 nm). For imaging, a microscope objective with magnifications of 20x and 40x were used to obtain a brighter field image of the UCNPs/graphene and UCNPs/glass. The acquired data was performed using the same optical system as for the PL measurements, analysed and plotted using PHySpecV2 and OriginPro softwares.

Chapter III

Results and Discussion

III.1 Microwave-assisted Synthesis and Characterization of $NaLnF_4$-based NPs

III.1.1 NP Growth and Phase Formation

A set of β-$NaGdF_4$:Yb^{3+}(20%), Er^{3+}(2%) @ $NaGdF_4$ and α-$NaGdF_4$:Yb^{3+}(20%), Er^{3+}(2%) @ $NaGdF_4$ oleate-capped NPs were synthesized via the established microwave-assisted synthesis [41, 44]. In this work, the crystalline phase was controlled by adjusting the molar ratio of Na^+-to-Ln^{3+} and reaction temperatures. This procedure was demonstrated by Halimi et al. [44], where hexagonal phase was obtained using a 3:1 ion ratio of Na^+:Ln^{3+}, however, the synthesis of cubic-phase requires only a 1:1 ion ratio of Na^+:Ln^{3+}. This method of NP synthesis was chosen because of its reproducibility in yielding the desired phase. The NP growth mechanism is illustrated in Figure III.1.

The NPs were developed during successive stages. For synthesizing core-only NPs, the precursor mixture was subjected to the microwave radiation with rapidly increasing temperature up to T_1. The stage (I) is described by a rapid nucleation of semi-soluble monomer units of the host lattice and the dopant material which ensues the stage (II).

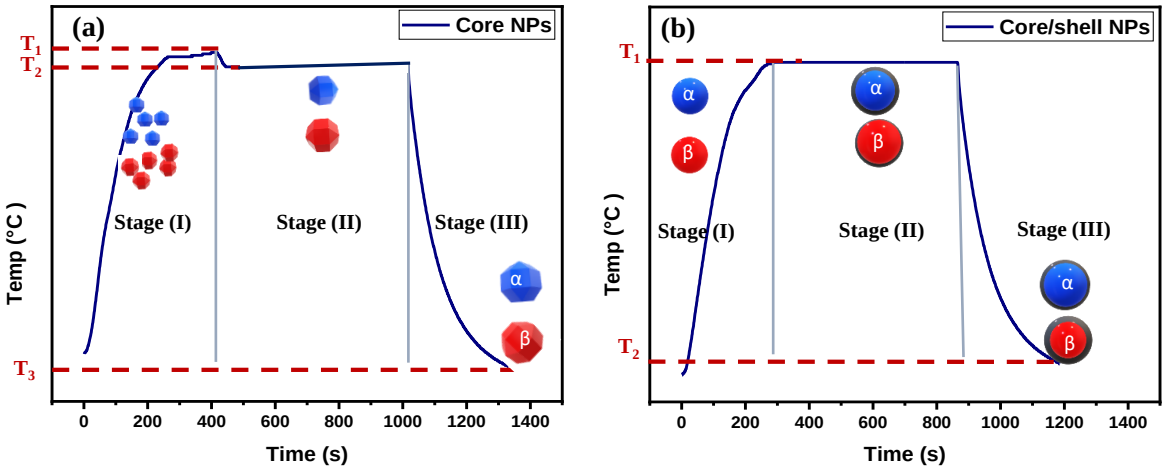

Figure III.1: Mechanism of nanoparticle growth under temperature profile. (a) α and β core-only NPs growth, (b) α and β shelling growth.

This phase starts by rapid cooling to a lower temperature T_2 then it continues for 10 min where, the formed nuclei undergo a particle growth [38]. The next step is the stage (III) defined by cooling down for 5 min to $T_3 = 50$ °C. Finally, the core only NPs were synthesized

During the synthesis of hexagonal phase NPs, T_1 and T_2 were set at 270 °C and 260 °C respectively. Whereas, for the cubic phase, they were set at 300 °C and 230 °C. The mechanism through which the NPs were developed is very similar to the basic principles of crystallization explained by LaMer plot [87–89].

For the shell growth, undoped α-$NaGdF_4$ shelling precursor was used whit a ratio 1:1 of Na^+:Gd^{3+}. For both crystalline phases, the mixture containing the core-only NPs that were previously prepared was subjected to heating up to $T_1 = 230$ °C where such nucleation of new NPs is no longer promoted, however, an epitaxial shell growth was performed. As a result, a core/shell NPs were obtained. The crystalline phase of core/shell NPs depends on the phase of the core-only NPs already involved in the reaction. This procedure of shell growth was developed by Hemmer's group [41, 44].

III.1.2 NP Characterization

III.1.2.1 Structural Characterization

The XRD patterns of hexagonal and cubic oleate-capped NPs are presented in Figure III.2. The XRD analysis confirms that the crystalline phase was controlled by the molar ratio of Na^{+}-to-Ln^{3+}. It is well known that in β-$NaGdF_4$, the Na^{+} has two selected sites in the cationic sublattice, while the Gd^{3+} ions have only one available sublattice site. However, in the α-$NaGdF_4$, there are no assigned sublattice sites and the Na^{+} and Gd^{3+} are randomly distributed across the crystal on the cations sites [41, 44, 90]. In this work, the preferential formation of the hexagonal phase of NPs can be attributed to the presence of the excess of Na^{+} ions. Notably, the components OA/ODE/OAm alone demonstrate limited proficiency as microwave absorbers, emphasizing the significance of the excess Na^{+} ions in facilitating the absorption of microwave energy and providing the necessary energy for for the crystallization process, thus favoring the emergence of the hexagonal phase. Tis is in agreemnet with previous work on the growth mechanism of sodium lanthanide fluoride NPs [41, 44, 90]. The XRD measurements confirm that the microwave-assisted approach is able to tune the selective growth of phase pure of $NaGdF_4$ NPs. Figure III.2 shows the XRD patterns of the represented NPs in both crystalline phases.

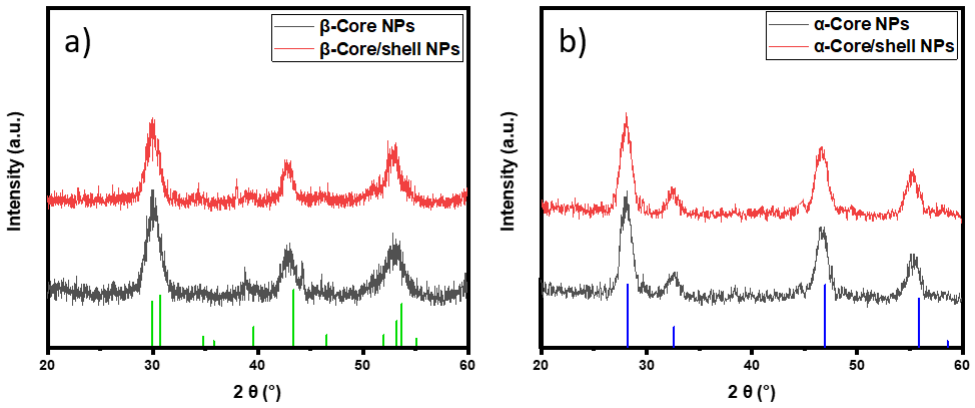

Figure III.2: Powder XRD patterns of a) hexagonal core and core/shell NPs, b) cubic core and core/shell NPs. References: green line β-$NaGdF_4$ (PDF card no. 01-080-8787), blue line α-$NaGdF_4$ (PDF card no. 00-027-0697).

Furthermore, the XRD analysis can also be utilized to estimate the crystallite size of NPs. The estimation of crystallite size is typically performed using the Scherrer equation, It relates the full width at half maximum (FWHM) of a diffraction peak, the wavelength of X-rays, and the crystallite size. The equation is as follows:

$$D = \frac{K\lambda}{\beta \cos\theta} \tag{III.1}$$

where:

D is the crystallite size, K is the shape factor, usualy, taken 0.94 for spherical nanoparticles in cubic and hexagonal phases [91, 92], λ is the wavelength of X-rays, β is the FWHM of the diffraction peak and θ is the Bragg angle. The determination of crystallite sizes was conducted for both phases of NPs, yielding results of approximately 6.5 $\pm$ 0.9 nm and 8.8 $\pm$ 1.0 nm correspondingly for β-core and β-core/shell NPs. However, the estimated crystallite sizes for the cubic phase were 7.0 $\pm$ 0.2 nm and 7.1 $\pm$ 0.5 nm respectively for α-core and α-core/shell NPs. The supporting data of the crystallite size calculation are presented in Appendix A. To investigate this further, a characterization by TEM was carried out.

The morphology of the synthesized $NaGdF_4$ NPs was determined by TEM and their size distributions were calculated using ImageJ and Origin8 software as displayed in Figure III.3 and Figure III.4. It can be seen from the TEM images in Figure III.3 (a, c) β-core and β-core/shell NPs and Figure III.4 (a,c) α-core NPs and α-core/shell NPs that all NPs were well monodispersed with uniform shapes. The estimated average sizes of the represented hexagonal NPs were found to be 7.1 $\pm$ 0.7 nm and 9.4 $\pm$ 0.8 nm for β-core and β-core/shell NPs, respectively as shown in Figure III.3 (b, d). On the other hand, for the represented cubic phase NPs, the average particle sizes were 6.6 $\pm$ 0.7 nm for core NPs and, 8.0 $\pm$ 0.8 nm for core/shell NPs as displayed in figure III.4 (b, d).The presence of a core/shell structure is further supported by the observed increase in particle size. The estimated shell thickness was calculated to be 1.15 nm for β-NPs and 0.7 nm for α-NPs. It is obvious that there was a good correlation between the mean dimensions of NPs determined by the TEM and the mean crystallite dimensions of NPs computed via the Scherer equation.

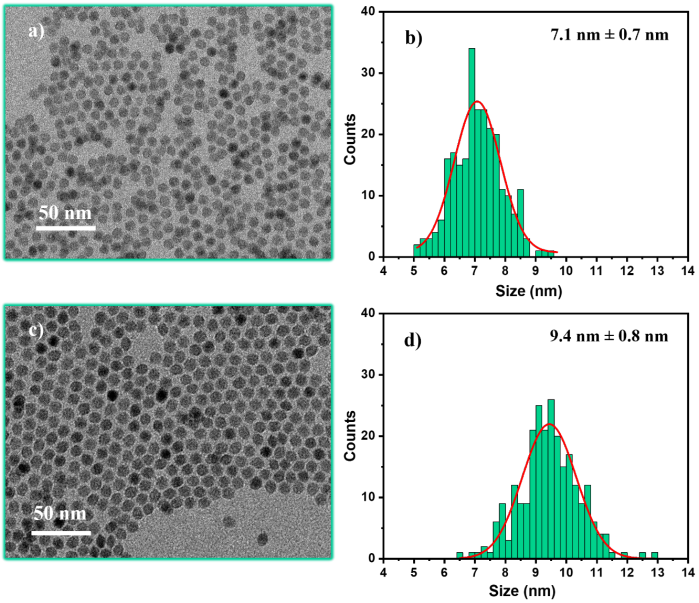

Figure III.3: TEM images and associated size distribution histograms of hexagonal NPs. (a,b) β-core NPs, (c,d) β-core/shell NPs.

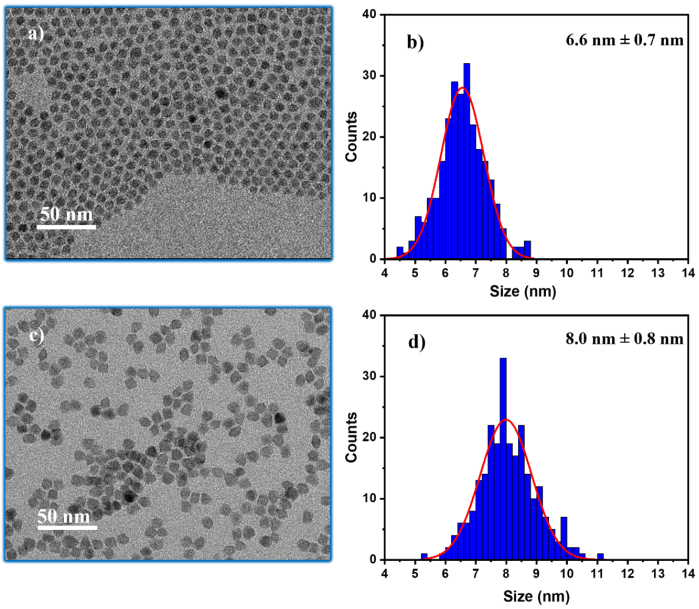

Figure III.4: TEM images and associated size distribution histograms of cubic NPs. (a,b) α-core NPs, (c,d) α-core/shell NPs.

After the preparation of nanoparticles, certain batches of β-NPs in core/shell structure underwent surface modifications to make them water-dispersible. Subsequently, second TEM measurements were conducted for the surface-modified NPs. The impact of the surface modifications is evident in Figure III.5. It is clear from Figures III.5 (a) and (b) that no changes occurred during the ligand removal process. The morphology of ligand-free NPs (LF-UCNPs) closely resembled that of OA-UCNPs. However, the TEM results revealed NP aggregation for both citrite-coated NPs (C-UCNPs) in Figure III.5 (d) and poly(acrylic acid)-NPs (PAA-UCNPNPs) in Figure III.5 (f). It is apparent that NP aggregation occurred in the last two cases, making the determination sizes of the surface-modified NPs challenging. To confirm the successful surface modification these NPs could be subjected to the Fourier-Transform Infrared Spectroscopy analysis.

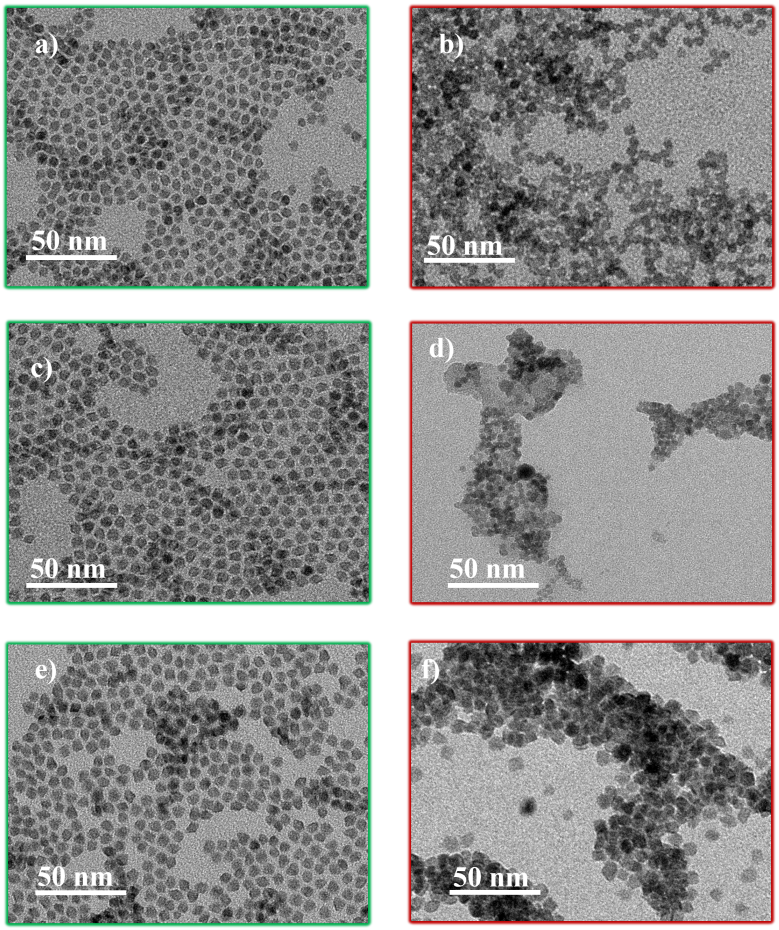

Figure III.5: TEM images of OA-UCNPs before and after surface modification. a), c), and e) are OA-UCNPs, b) is LF-UCNPs, d) is C-UCNPs, and f) is PAA-UCNPs.

III.1.2.2 Optical Characterization

To study the upconversion emission of the synthesized NPs, PL spectra of NPs dispersed in hexane (about 5 mg/mL) were conducted under 980 nm NIR laser excitation. For instance, Figure III.6 shows the emission spectra of core and core/shell NPs. All dispersed NPs showed upconverted emission peaks in the green and red spectral regions. Specifically, the peaks centered at 525 nm, 550 nm and 660 nm were assigned to $^2H_{11/2} \rightarrow {}^4I_{15/2}$, $^4S_{3/2} \rightarrow {}^4I_{15/2}$, and $^4F_{9/2} \rightarrow {}^4I_{15/2}$ transitions of Er^{3+}, respectively [29, 44, 93–97].

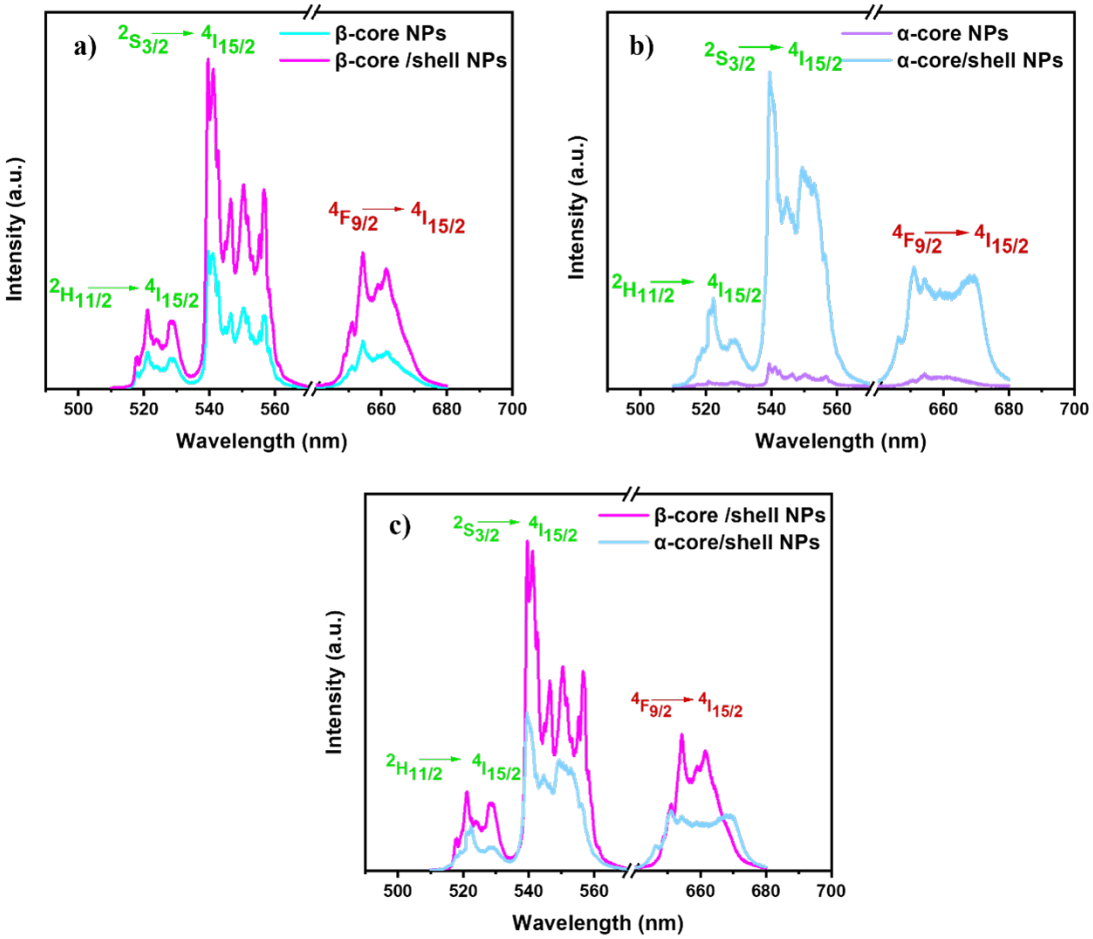

Figure III.6: PL spectra of NPs dispersed in hexane. a) β-phase NPs, b) α-phase NPs, and c) comparison between β and α NPs in core/shell architecture. $^2H_{11/2} \rightarrow {}^4I_{15/2}$, $^4S_{3/2} \rightarrow {}^4I_{15/2}$, and $^4F_{9/2} \rightarrow {}^4I_{15/2}$ are transitions of Er^{3+}. All spectra were obtained under 980 nm laser excitation.

As seen from Figure III.6 (a and b), the core/shell NPs architecture shows a brighter upcoversion emission than the core-only NPs for both crystalline phases. The shell growth increases the emission intensity by reducing the surface quenching effects [40, 94]. However, the core/shell NPs in hexagonal phase displays a higher emission compared to the one in cubic phase as shown in Figure III.6 c). This is because the hexagonal phase has low crystal symmetry which allows a stronger coupling between 4f energy levels leading to a higher UC emission efficiency. Furthermore, the hexagonal phase is characterized by low-energy phonons, which helps to minimize the non-radiative relaxations. This is in agreement with previous works [44, 98]. In fact, for hexagonal phase, the upcoversion emission was improved to the point that it became more visible to the naked eye under excitation using a handheld NIR laser pointer with power of 50 mW as shown in Figure III.7.
It is important to note that the ideal shell thickness can vary depending on the specific UCNPs and application, and may require optimization through experimental evaluation.

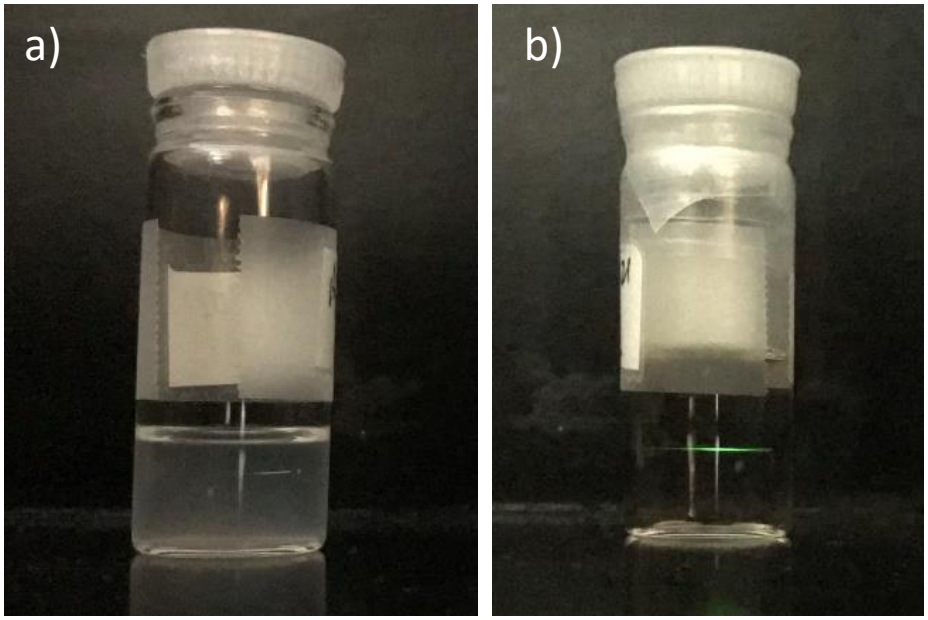

Figure III.7: Digital image of green light from NPs dispersed in hexane under excitation by hand hold NIR laser pointer with power of 50 mW, a) β-core NPs and b) β-core/shell NPs

To assess the effect of surface modification on the optical properties of NPs, PL spectra of the OA-UCNPs, LF-UCNPs, C-UCNPs and PAA-UCNPs dispersed in ethanol (5 mg/mL)

were represented in Figure III.8. The modified-surface NPs were emitting, as expected, in the green and red spectral regions at wavelengths 525, 550, and 660 nm under 980 nm excitation. Comparing the emissions of surface modified NPs,however, the quenching process can be seen in LF-UCNPs as the solvent is in contact directly with their surface causing a luminescence quenching. Moreover, the emission of PAA-UCNPs was very low compared to other modified-surface NPs. This might be due to the surface passivation effected by the PAA leading to a lower emission intensity. At this point, the OA-UCNPs are the best emitter and they will be used for the rest of this work.

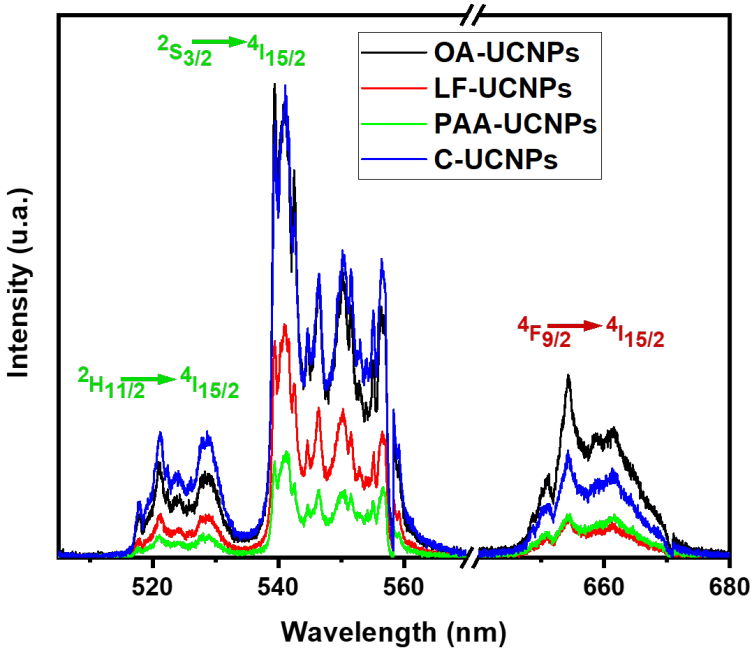

Figure III.8: PL spectra of OA-UCNPs, LF-UCNPs, PAA-UCNPs, and C-UCNPs in ethanol, dispersions (5 mg/mL) under 980 nm laser excitation.

III.2 Graphene-UCNPs Hybrid System: Preparation and Characterization

In this section, the graphene–nanoparticle hybrid materials were prepared and characterized. First, the route used to prepare a hybrid system was by drop-casting a dispersed NPs in hexane (16 mg/mL) on graphene film already transferred on a glass substrate. Figure III.9 displays the top view optical microscope images of the graphene before its combination with UCNPs.

The bright-field images reveal that the graphene film was successfully transferred on the glass substrate. Moreover, Figure III.9 a) shows several micrometres of the graphene edge on the glass indicating its adhesion. Furthermore, Figures III.9 b) and c) prove that there were no significant wrinkles or cracks in the graphene film, but few small spots which disappear towards the middle of the film. These defects might be an air bubbling trapped

between the graphene and the glass during the transfer procedure. Besides, Figure III.9 d) shows a residue which most probably is the PMMA. It is very important to make sure that all PMMA layer dissolved in acetone to obtain a clean graphene film. In order to verify the cleanliness of the graphene film with respect to residual contaminants, it is advisable to conduct further characterization through Raman spectroscopy.

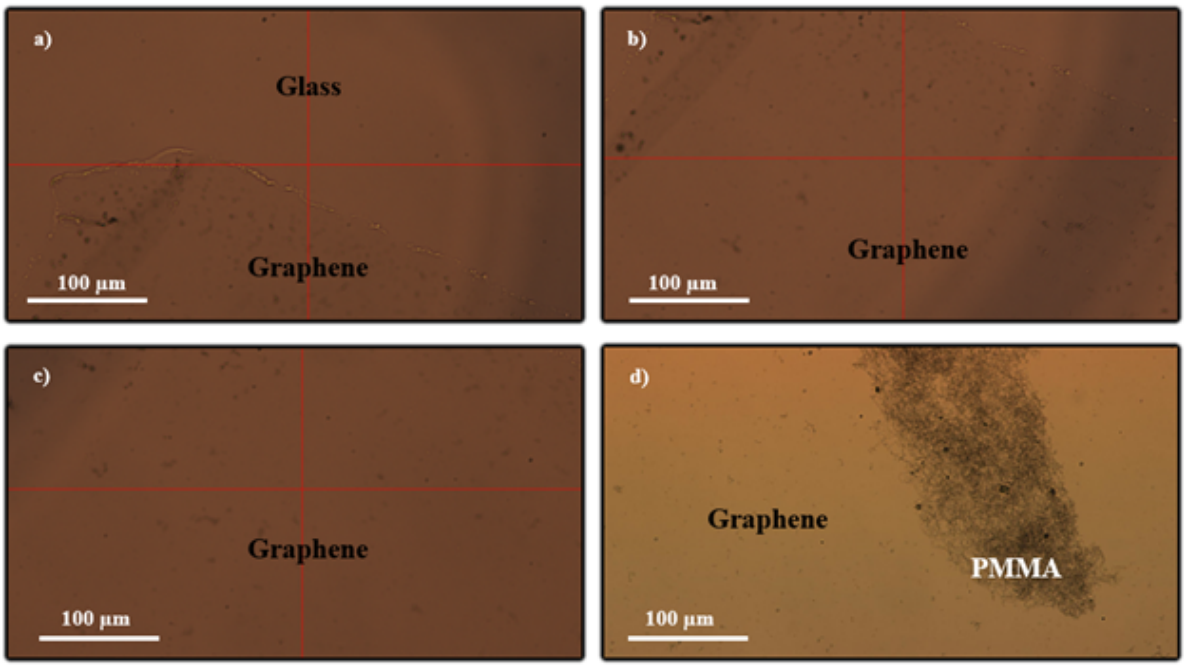

Figure III.9: Optical microscope images of graphene on glass. a) Edges of graphene on glass, b) and c) graphene on glass, and d) PMMA residue on graphene.

To study the distribution of the UCNPs on both graphene and glass and to investigate their corresponding optical characteristics, bright-field images within the region of interest (ROI) associated with photoluminescence spectra from randomly chosen spots were extracted as shown in Figure III.10. The bright-field images in Figures III.10 and III.11 show an heterogeneous spread of UCNPs on graphene and glass. Some areas show NPs aggregations on the surface, i.e., spots 2 and 3 on graphene in Figure III.10 and spots 1 and 3 on glass in Figure III.11, where their associated emissions are very bright. On the other regions where the distribution of NPs is relatively homogeneous (less aggregation), spots 1 and 4 on graphene in Figure III.10 and spots 2 and 4 on glass in Figure III.11 present a lower emissions intensity.

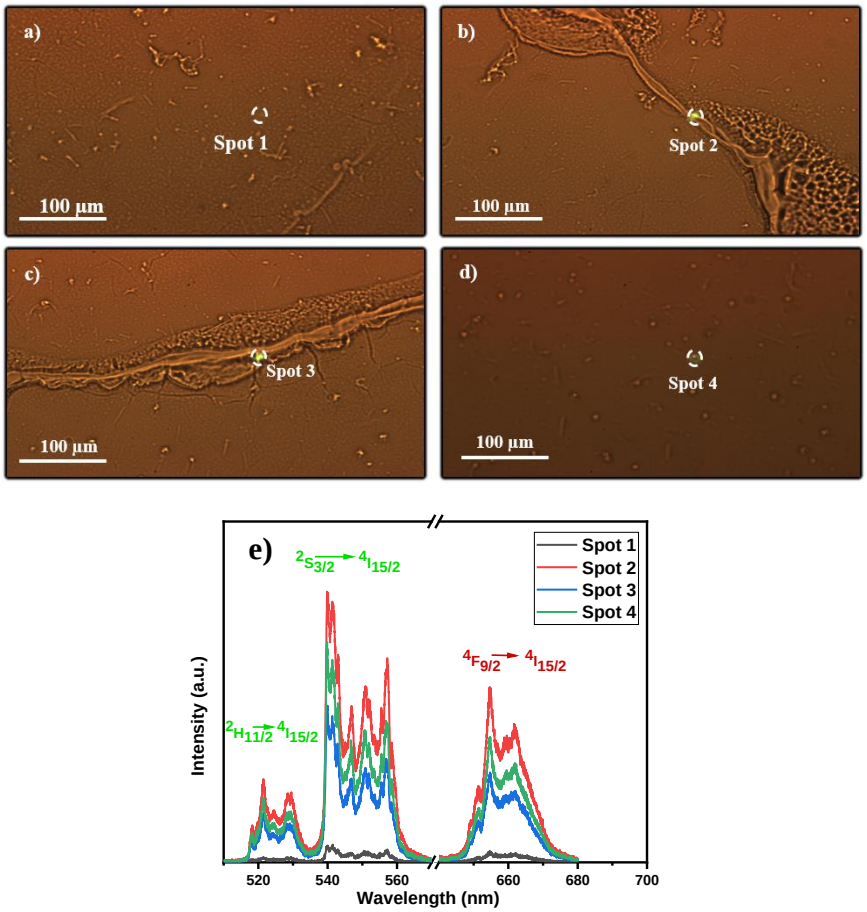

Figure III.10: Bright-field images associated with PL spectra of UCNPs/Graphene, a) microscope image of ROI 1, b) microscope image of ROI 2, c) microscope image of ROI 3, d) microscope image of ROI 4, and e) PL spectra of different spots.

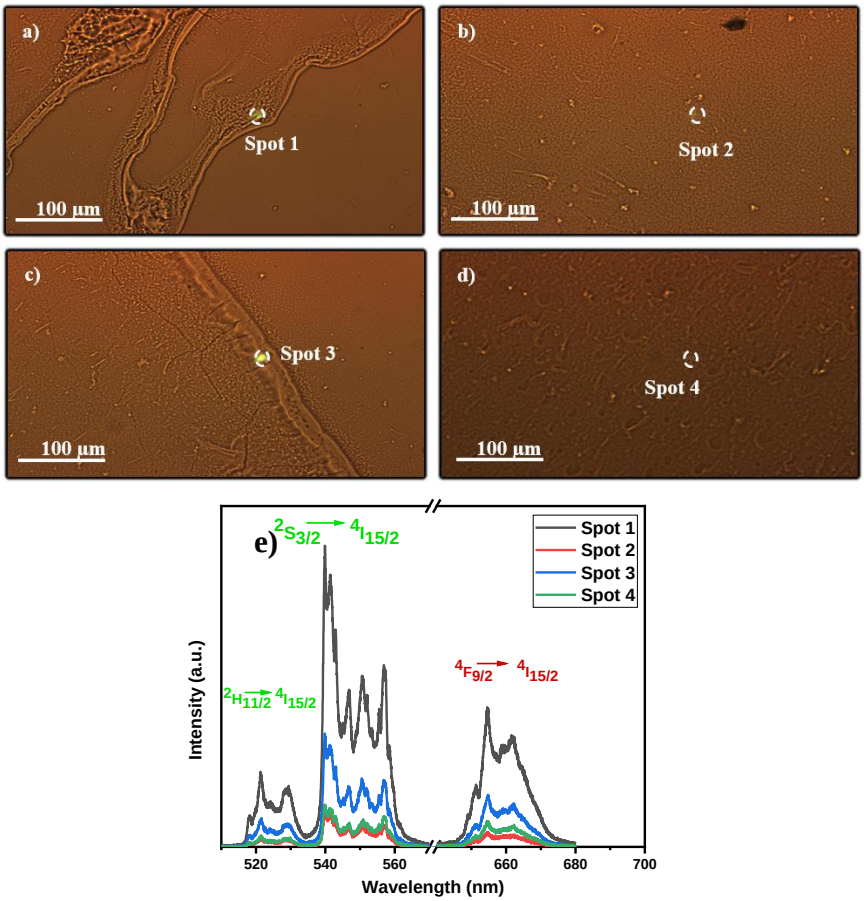

Figure III.11: Bright-field images associated with PL spectra of UCNPs/Glass, a) microscope image of ROI 1, b) microscope image of ROI 2, c) microscope image of ROI 3, d) microscope image of ROI 4, and e) PL spectra of different spots.

To alleviate the potential influence of abnormally emissive regions on the extracted spectral data, averaging of photoluminescence spectra was performed for UCNPS/Graphene and UCNPs/Glass, as illustrated in Figure III.12. It is clearly seen that the PL averaging intensities of UCNPs/graphene overlap the PL averaging intensities of UCNPs/Glass.

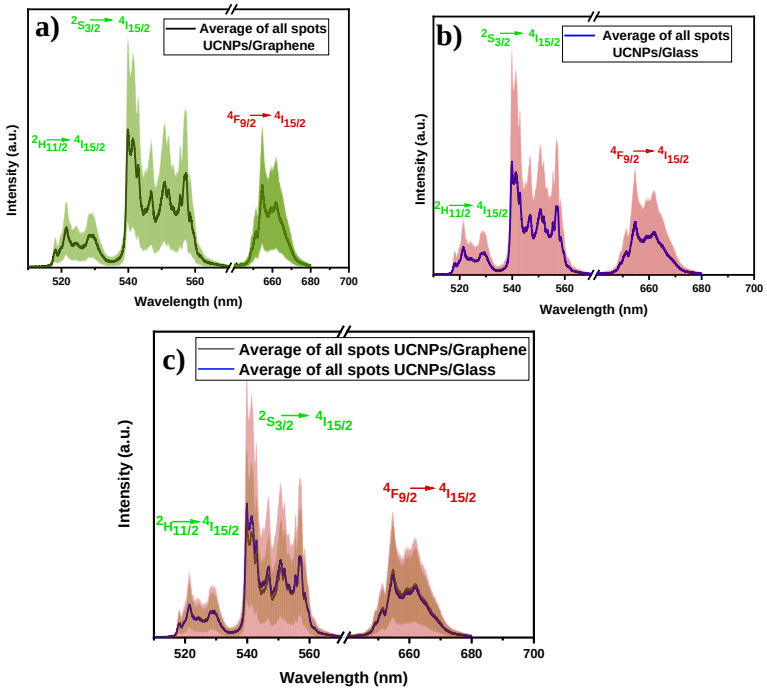

Figure III.12: Average PL spectra of all spots, a) for UCNPs/Graphene, b) for UCNPs/Glass, c) comparison between PL averaging. Shadows on graphs are standard deviations. Laser excitation (λ = 980 nm).

Summarising all the PL spectra for the first attempt, where UCNPs were deposited by drop-casting method, the overlap of photoluminescence (PL) averaging intensities between UCNPs/graphene and UCNPs/Glass is evident from the observation. This is conclude that there was no interaction between UCNPs and graphene as expected. This could be caused by the heterogeneity of NPs distribution. Depositing NPs on graphene by drop-casting method is not a good route to get a homogeneous and thin film of NPs. Subsequently, the spin-coater was used in preparing the hybrid system to overcome the aforementioned problem.

As a second attempt, to enhance the deposition quality of UCNPs on graphene, hybrid systems were prepared using a spin-coater. Specifically, HSI and PL measurements were extracted from scanned 10 μm x 10 μm areas of both UNCPs/graphene and UCNPs/glass to to assess their respective emission intensities. Four areas from each were scanned. Figures III.13 and III.14 show the first areas scanned of UCNPs/Graphene and UCNPs/Glass, respectively. The remaning scanned areas (Area 2, Area 3 and Area 4) from each are shown

in the Appendix B.

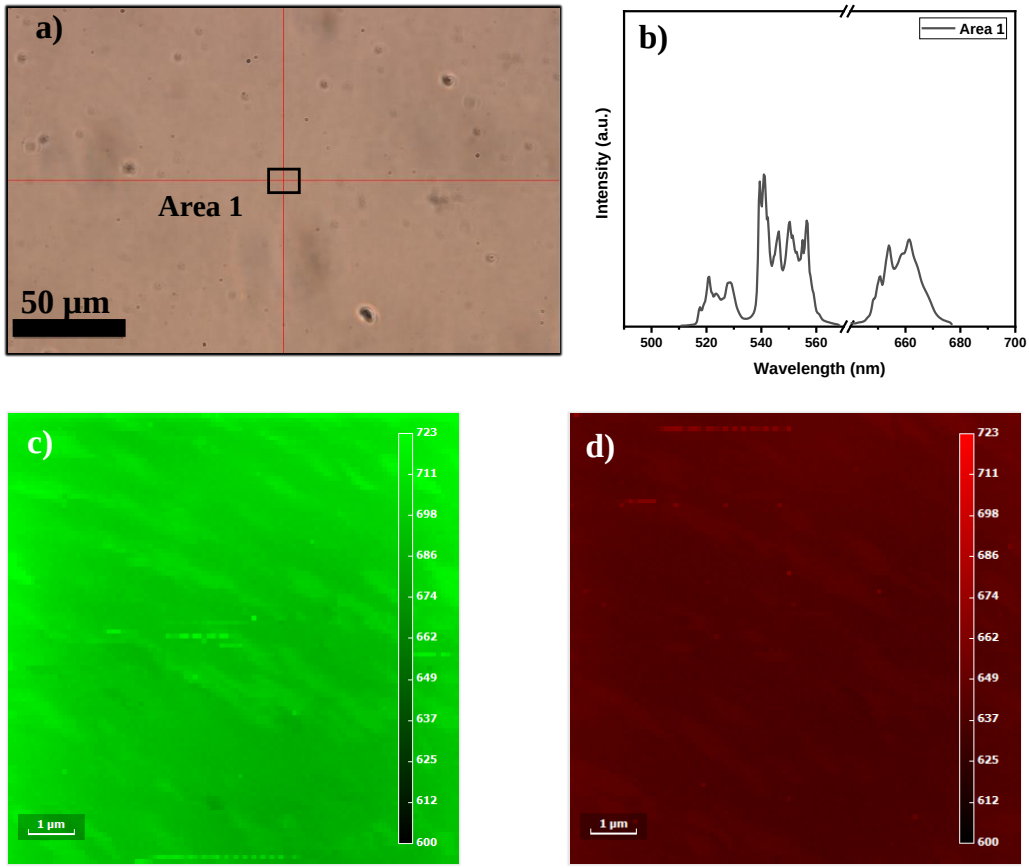

Figure III.13: a) Bright-field image of UCNPs/Graphene, b) PL spectra of the scanned area 1, c) spectral image associated to the green emission (525 nm and 550 nm), and d) spectral image associated to the red emission (660 nm). The black square represents the area of hyperspectral imaging.

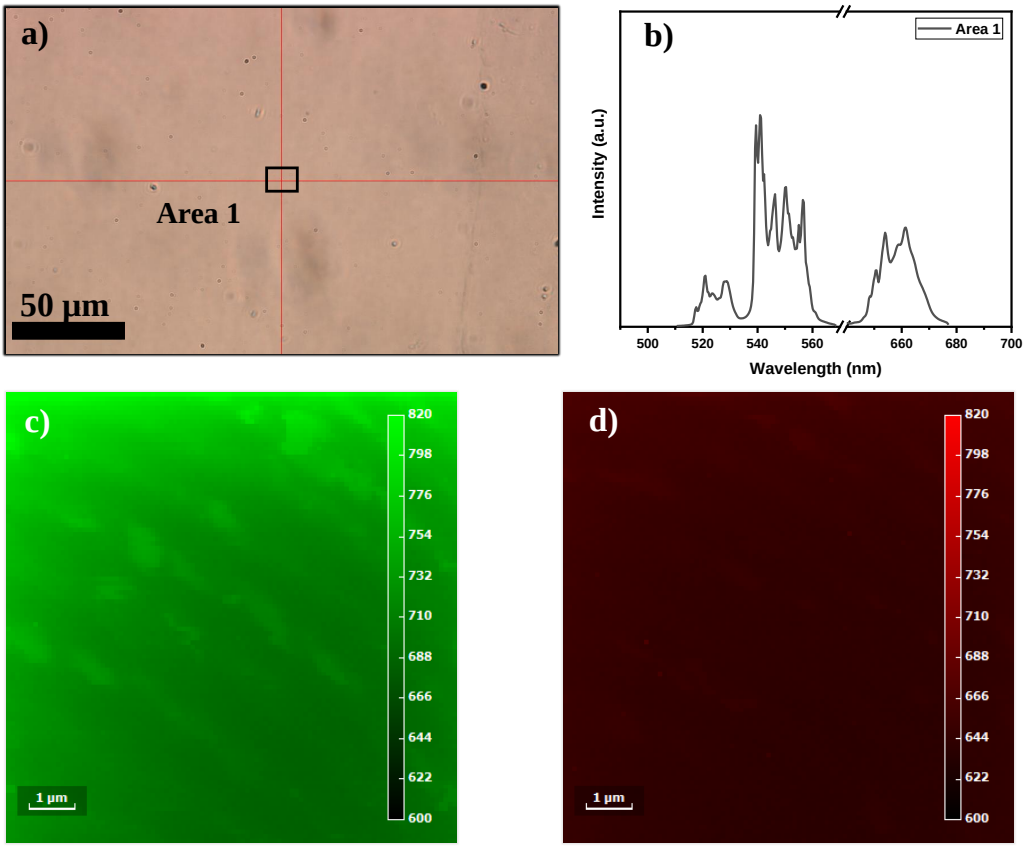

Figure III.14: a) Bright-field image of UCNPs/Glass, b) PL spectra of the scanned area 1, c) spectral image associated to the green emission (525 nm and 540 nm) and, d) spectral image associated to the red emission (660 nm). The black square represents the area of hyperspectral imaging.

The bright-field images obtained by the microscope of each scanned area show a quite homogeneous distribution of PL. Based on this result, it is evident that the NP films were more homogeneous than the ones obtained by drop-coasting. Comparing the averaging PL spectra of all probed areas showed in Figure III.15, it can be seen that the emission intensities remain unchanged regardless of whether UCNPs/Graphene or UCNPs/Glass. This indicates that there was no energy transfer between UCNPs and graphene.

These results are against what was expected from previous work where they combined $NaYF_4$: Yb^{3+}, Er^{3+}, Nd^{3+} @ $NaYF_4$: Nd^{3+} and $NaYF_4$: Yb^{3+}, Tm^{3+} @ $NaYF_4$ core/shell UCNPs with graphene [9, 48, 78]. In their work, these UCNPs were crystallized in the hexagonal phase with a diameter between 20 and 30 nm. When the hybrid device subjected to 808 or 980 nm laser illumination, the photoluminescence spectra of UCNPs/Graphene

showed a considerable reduction in the upcoversion emission compared to the UCNPs without graphene. The quenching of the photoluminescence intensities was explained by a charge transfer occurring between UCNPs and graphene after a laser illumination. According to other published work in [93], the fluorescence of the core-UCNPs was quenched in contact with graphene under 980 nm laser excitation. The fluorescence quenching was explained by the charge transfer from the core-NPs to the Fermi level of the graphene. For their work, the average diameter of core-NPs was 17 ± 2 nm.

The lack of interaction between UCNPs and graphene in my work could be attributed to the poor quality of the graphene film.This is because there was no characterization performed on it, or it could be related to the size of the NPs or the thickness of the shell.

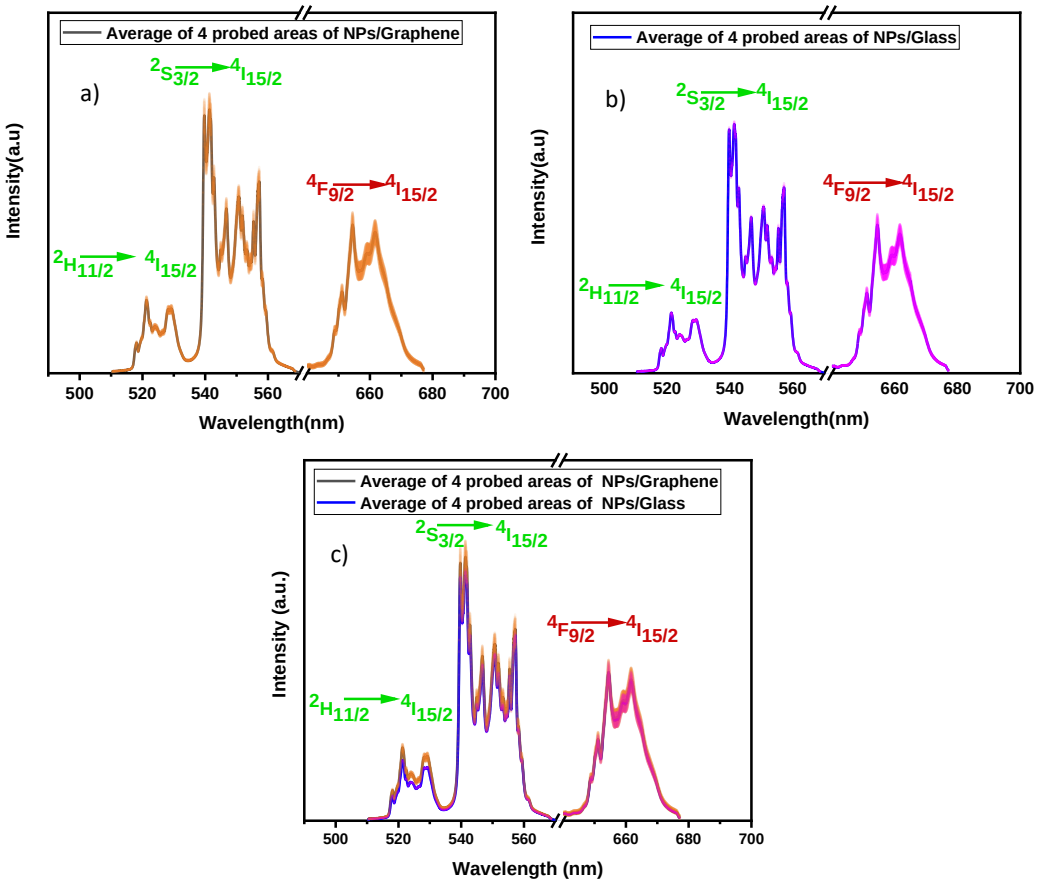

Figure III.15: Average PL spectra of all areas, a) for UCNPs/Graphene, b) for UCNPs/Glass, c) comparison between PL averaging. Shadows on graphs are standard deviations. Laser excitation (λ = 980 nm, P = 150 mW).

Chapter IV

Conclusions

In summary, the synthesis of $NaGdF_4$ NPs was successfully achieved via microwave assisted synthesis using [$(LnTFA)_3$] as a precursor and a soduim source following established protocols. The crystalline phase was controlled by the molar ratio of Na^+-to-$Ln^{3+}$and the reaction temperature. β-$NaGdF_4$:Yb^{3+}(20%), Er^{3+}(2%) @ $NaGdF_4$ and α-$NaGdF_4$:Yb^{3+}(20%), Er^{3+}(2%) @ $NaGdF_4$ oleate-capped nanoparticles were used in this work. The preferred option for light emission in the visible region involves the crystallization of $NaGdF_4$:Yb^{3+}, Er^{3+} core/shell UCNPs in the hexagonal phase. The homogeneous films of a hybrid UCNPs/Graphene samples were obtained using a spin-coater. The optical study of the UCNPs/graphene did not show any potential interaction. Based on the obtained results and previous published works, in order to gain a deeper understanding of the interaction between UCNPs/graphene, it is essential to study nanoparticles (NPs) with an optimal shelling structure, such as core/shell/shell NPs, as well as the optimal sizes of core-NPs and core/shell-NPs. Also, the impact of NPs modified surface on the graphene films should be studied. Furthermore, a microscope analysis and structural characterization using techniques such as Atomic Force Microscopy (AFM) and Raman Spectroscopy are essential for evaluating the graphene film and to study the distribution of NPs on the graphene. The photocurrent mapping measurement can be a good asset to understand any energy transfer between the UCNPs and graphene.

APPENDICES

Appendix A

Appendix for Crystallite Size

Table A.1: Crystallite size of NPs

	Peak Position 2 θ	**FWHM**	**Crystallite Size D (nm)**	**Crystallite Size Average (nm)**	**Standard Deviation**
β-core NPs	30.04	1.58	5.46	6.51	0.88
	42.91	1.16	7.63		
	52.91	1.43	6.44		
β-core/shell NPs	29.85	1.22	7.01	8.78	1.04
	42.74	0.83	10.63		
	52.73	1.06	8.71		
α-core NPs	28.06	1.28	6.66	6.97	0.24
	32.50	1.18	7.28		
	46.64	1.30	6.93		
	55.31	1.30	7.19		
α-core/shell NPs	28.03	1.28	6.62	7.06	0.54
	32.47	1.08	7.95		
	46.60	1.36	6.62		
	55.23	1.32	7.06		

Appendix B

Appendix for HSI Results

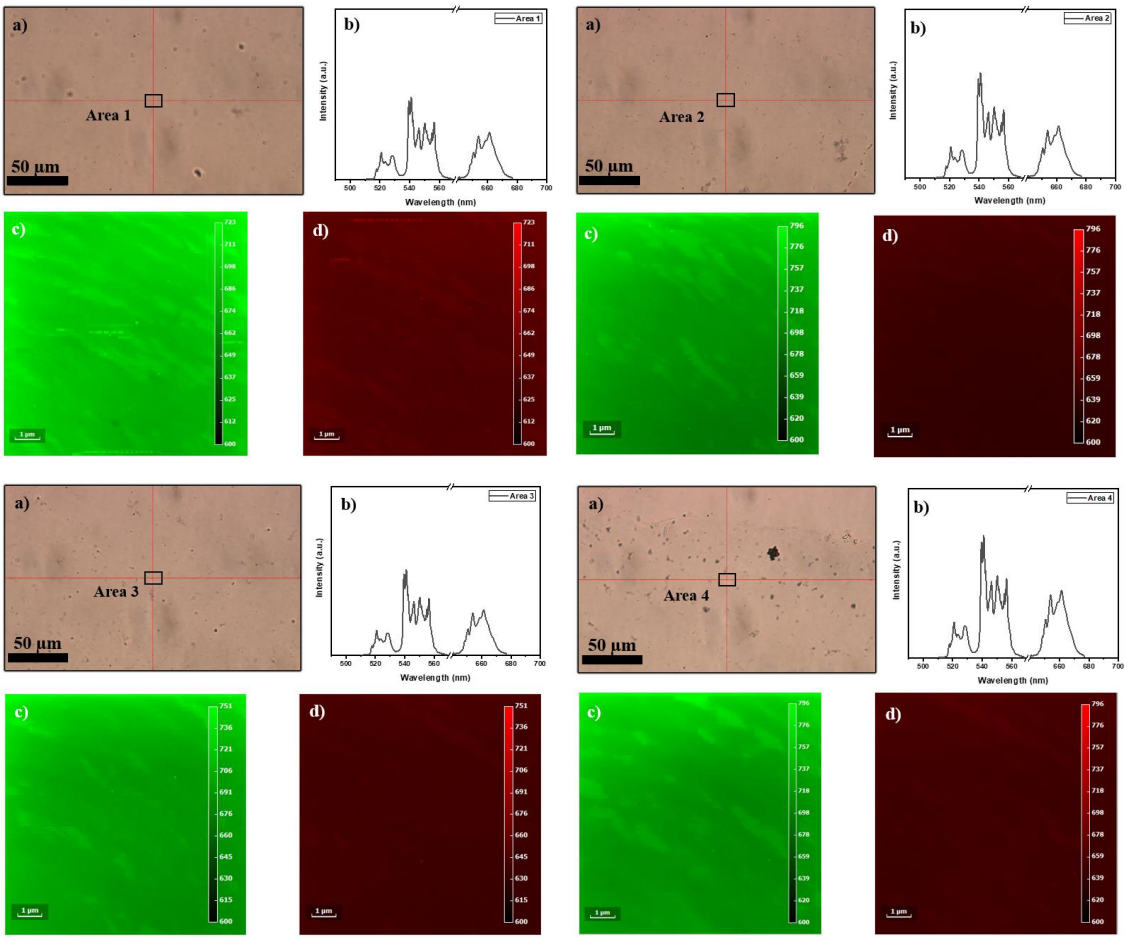

Figure B.1: Four scanned areas on UCNPs/Graphene. a) Bright-field image of UCNPs/Graphene, b) PL spectra of the scanned area, c) spectral image associated to the green emission and, d) spectral image associated to the red emission. The black square represents the area of hyperspectral imaging.

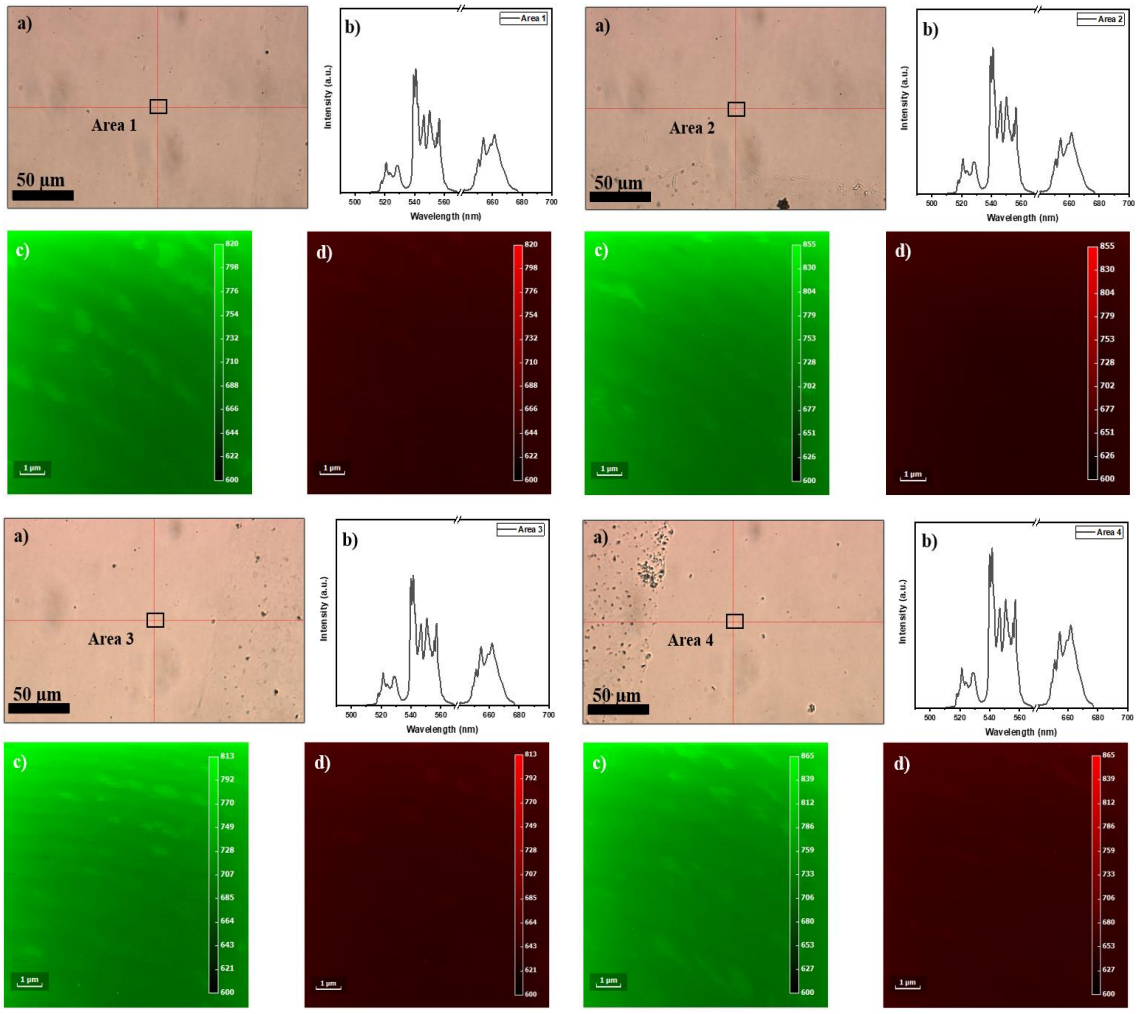

Figure B.2: Four scanned areas on UCNPs/Glass. a) Bright-field image of UCNPs/Glass, b) PL spectra of the scanned area, c) spectral image associated to the green emission and, d) spectral image associated to the red emission. The black square represents the area of hyperspectral imaging

References

[1] P. Dinér, "Yttrium from Ytterby", *Nat. Chem.*, 2016, **8** (2), 192–192.

[2] S. Cotton, *Lanthanide and Actinide Chemistry*, West Sussex: John Wiley & Sons, 2013.

[3] H. Dong, L.-D. Sun, and C.-H. Yan, "Basic understanding of the lanthanide related upconversion emissions", *Nanoscale*, 2013, **5** (13), 5703–5714.

[4] M. Shahrukh, "Rational design and synthesis of sub-15 nm upconverting nanoparticles for improved LRET efficiency", Msc Thesis, University of Toronto (Canada), 2018.

[5] D. Li, H. Ågren, and G. Chen, "Near infrared harvesting dye-sensitized solar cells enabled by rare-earth upconversion materials", *Dalton Tran.*, 2018, **47** (26), 8526–8537.

[6] S. C. Ray, "Chapter 2 - Application and Uses of Graphene Oxide and Reduced Graphene Oxide", in: *Applications of Graphene and Graphene-Oxide Based Nanomaterials*, ed. by S. C. Ray, Micro and Nano Technologies, Oxford: William Andrew Publishing, 2015, 39–55.

[7] P. T. Yin, S. Shah, M. Chhowalla, and K.-B. Lee, "Design, synthesis, and characterization of graphene–nanoparticle hybrid materials for bioapplications", *Chem. Rev.*, 2015, **115** (7), 2483–2531.

[8] J. Wu, Z. Yang, C. Qiu, Y. Zhang, Z. Wu, J. Yang, Y. Lu, J. Li, D. Yang, R. Hao, et al., "Enhanced performance of a graphene/GaAs self-driven near-infrared

photodetector with upconversion nanoparticles", *Nanoscale*, 2018, **10** (17), 8023–8030.

[9] M. Kataria, K. Yadav, S.-Y. Cai, Y.-M. Liao, H.-I. Lin, T. L. Shen, Y.-H. Chen, Y.-T. Chen, W.-H. Wang, and Y.-F. Chen, "Highly sensitive, visible blind, wearable, and omnidirectional near-infrared photodetectors", *ACS Nano*, 2018, **12** (9), 9596–9607.

[10] A. Gupta, M. K. Thakur, T. A. Effendi, R.-S. Chen, H.-Y. Cheng, K.-H. Lin, M. Bouras, D. S. Tomar, H. Y. Kuo, and S. Chattopadhyay, "Metallo-graphene enhanced upconversion luminescence for broadband photodetection under polychromatic illumination", *Chem. Eng. J.*, 2021, **420**, 127608.

[11] I. Khalil, N. M. Julkapli, W. A. Yehye, W. J. Basirun, and S. K. Bhargava, "Graphene–gold nanoparticles hybrid—synthesis, functionalization, and application in a electrochemical and surface-enhanced raman scattering biosensor", *Materials*, 2016, **9** (6), 406.

[12] P. Pyykkö, "Magically magnetic gadolinium", *Nat. Chem.*, 2015, **7** (8), 680–680.

[13] R. Anwander, "Lanthanide amides", *Organolanthoid Chemistry: Synthesis, Structure, Catalysis*, 1996, 33–112.

[14] J. E. Huheey, E. A. Keiter, and Keiter, *Inorganic Chemistry: Principles of Structure and Reactivity*, New York: Harper & Row, 1997.

[15] C. C. Peterson, D. A. Penchoff, J. D. Auxier, and H. L. Hall, "Establishing cost-effective computational models for the prediction of lanthanoid binding in $[Ln(NO_3)]^{2+}$(with Ln = La to Lu)", *ACS Omega*, 2019, **4** (1), 1375–1385.

[16] K. Binnemans and C. Görller-Walrand, "On the color of the trivalent lanthanide ions", *Chem. Phys. Lett.*, 1995, **235** (3), 163–174.

[17] R. D. Peacock, "The intensities of lanthanide f f transitions", in: *Rare Earths*, Springer, 1975, 83–122.

[18] J. Wang, F. Wang, J. Xu, Y. Wang, Y. Liu, X. Chen, H. Chen, and X. Liu, "Lanthanide-doped $LiYF_4$ nanoparticles: Synthesis and multicolor upconversion tuning", *Comptes Rendus Chimie*, 2010, **13** (6-7), 731–736.

[19] J.-C. G. Bünzli and C. Piguet, "Taking advantage of luminescent lanthanide ions", *Chem. Soc. Rev.*, 2005, **34** (12), 1048–1077.

[20] J.-C. Bünzli and S. Eliseeva, "Basics of Lanthanide Photophysics", in: vol. 7, Berlin Heidelberg: Springer, July 2010, pp. 1–45.

[21] L Eyring, K. A. Gschneidner, and G. Lander, *Handbook on the Physics and Chemistry of Rare Earths*, vol. 32, North Holland: Elsevier, 2002.

[22] F. Artizzu, "Near-Infrared Luminescent Lanthanide Complexes of Quinolinol Ligands: Structure/Properties Relationship", PhD dissertation, Università degli Studi di Cagliari (Italy), 2008.

[23] L.-D. Sun, H. Dong, P.-Z. Zhang, and C.-H. Yan, "Upconversion of rare earth nanomaterials", *Annu. Rev. Phys. Chem*, 2015, **66** (1), 619–642.

[24] J. Liao, "Optical fingerprints of upconversion nanoparticles for super-capacity multiplexing", PhD Thesis, University of Technology Sydney (Australia), 2020.

[25] Y. Huang, "Upconverting nanoparticles for integration in bioimaging and therapeutic applications.", PhD thesis, Université du Québec, Institut national de la recherche scientifique, 2017.

[26] S. Boddu, "Synthesis and characterization of lanthanide ions doped nanomaterials", *A PhD thesis, Homi Bhabha National Institute, Mumbai*, 2011,

[27] M. V. DaCosta, S. Doughan, Y. Han, and U. J. Krull, "Lanthanide upconversion nanoparticles and applications in bioassays and bioimaging: A review", *Anal. Chim. Acta*, 2014, **832**, 1–33.

[28] S. Sarkar, B. Meesaragandla, C. Hazra, and V. Mahalingam, "Sub-5 nm Ln^{3+}-doped $BaLuF_5$ nanocrystals: a platform to realize upconversion via interparticle energy transfer (IPET)", *Ad. Mat.*, 2013, **25** (6), 856–860.

[29] Y. Sun, "Surface Conjugation of Upconversion Nanoparticles via Supramolecular Host-guest Self-assembly", PhD dissertation, University of Technology Sydney (Australia), 2018.

[30] M Ding and D Chen, "Lanthanide ions doped upconversion nanomaterials: synthesis, surface engineering, and application in drug delivery", in: *Nanoarchitectonics for Smart Delivery and Drug Targeting*, William Andrew Applied Science Publishers, 2016, 227–260.

[31] R. Quimby, N. Condon, S. O'Connor, S Biswal, and S. Bowman, "Upconversion and excited-state absorption in the lower levels of Er: KPb_2Cl_5", *Opt. Mat.*, 2008, **30** (6), 827–834.

[32] M.-F. Joubert, "Photon avalanche upconversion in rare earth laser materials", *Opt. Mat.*, 1999, **11** (2-3), 181–203.

[33] A. Singh, K Kumar, A. Pandey, O Parkash, S. Rai, and D Kumar, "Photon avalanche upconversion and pump power studies in LaF_3: Er^{3+}/Yb^{3+} phosphor", *App. Phys.*, 2011, **104** (4), 1035–1041.

[34] F. Wang, R. Deng, J. Wang, Q. Wang, Y. Han, H. Zhu, X. Chen, and X. Liu, "Tuning upconversion through energy migration in core–shell nanoparticles", *Nat. Mater.*, 2011, **10** (12), 968–973.

[35] L. Cheng, C. Wang, and Z. Liu, "Upconversion nanoparticles and their composite nanostructures for biomedical imaging and cancer therapy", *Nanoscale*, 2013, **5** (1), 23–37.

[36] V. Utochnikova and N. Kuzmina, "Photoluminescence of lanthanide aromatic carboxylates", *Rus. J. Coord. Chem.*, 2016, **42** (10), 679–694.

[37] M. H. Werts, "Making sense of lanthanide luminescence", *Sci. Prog.*, 2005, **88** (2), 101–131.

[38] I. Halimi, "Energy Transfer in Lanthanide-based Nanomaterials", Msc Thesis, University of Ottawa (Canada), 2020.

[39] F. Zhang, *Photon Upconversion Nanomaterials*, vol. 416, Berlin Heidelberg: Springer-Verlag, 2015.

[40] F. Wang, Y. Han, C. S. Lim, Y. Lu, J. Wang, J. Xu, H. Chen, C. Zhang, M. Hong, and X. Liu, "Simultaneous phase and size control of upconversion nanocrystals through lanthanide doping", *Nature*, 2010, **463** (7284), 1061–1065.

[41] N. Liu, R. Marin, Y. Mazouzi, G. O. Cron, A. Shuhendler, and E. Hemmer, "Cubic versus hexagonal–effect of host crystallinity on the T_1 shortening behaviour of $NaGdF_4$ nanoparticles", *Nanoscale*, 2019, **11** (14), 6794–6801.

[42] A. Herrmann, M. Tylkowski, C. Bocker, and C. Russel, "Cubic and hexagonal $NaGdF_4$ crystals precipitated from an aluminosilicate glass: preparation and luminescence properties", *Chem. Mat.*, 2013, **25** (14), 2878–2884.

[43] N. Liu, N. Gobeil, P. Evers, I. Gessner, E. M. Rodrigues, and E. Hemmer, "Water dispersible ligand-free rare earth fluoride nanoparticles: water transfer versus $NaREF_4$-to-REF_3 phase transformation", *Dalton Trans.*, 2020, **49** (45), 16204–16216.

[44] I. Halimi, E. M. Rodrigues, S. L. Maurizio, H.-Q. T. Sun, M. Grewal, E. M. Boase, N. Liu, R. Marin, and E. Hemmer, "Pick your precursor! Tailoring the size and crystal phase of microwave-synthesized sub-10 nm upconverting nanoparticles", *J. Mater. Chem.*, 2019, **7** (48), 15364–15374.

[45] G. Chen, H. Qiu, P. N. Prasad, and X. Chen, "Upconversion nanoparticles: design, nanochemistry, and applications in theranostics", *Chem. Rev.*, 2014, **114** (10), 5161–5214.

[46] M. Haase and H. Schäfer, "Upconverting nanoparticles", *Angew. Chem., Int. Ed.*, 2011, **50** (26), 5808–5829.

[47] F. Wang and X. Liu, "Upconversion multicolor fine-tuning: visible to near-infrared emission from lanthanide-doped $NaYF_4$ nanoparticles", *J. Am. Chem. Soc.*, 2008, **130** (17), 5642–5643.

[48] S. Y. Lee, G. Lee, Y.-S. Jun, and Y. I. Park, "Visible/near-infrared driven highly efficient photocatalyst based on upconversion nanoparticles/g-C_3N_4 nanocomposite", *App. Sur. Sci.*, 2020, **508**, 144839.

[49] M. Khatami, H. Q. Alijani, M. S. Nejad, and R. S. Varma, "Core@ shell nanoparticles: greener synthesis using natural plant products", *App. Sci*, 2018, **8** (3), 411.

[50] G. Chen, H. Ågren, T. Y. Ohulchanskyy, and P. N. Prasad, "Light upconverting core–shell nanostructures: nanophotonic control for emerging applications", *Chem. Soc. Rev.*, 2015, **44** (6), 1680–1713.

[51] N. J. Johnson, A. Korinek, C. Dong, and F. C. van Veggel, "Self-focusing by Ostwald ripening: a strategy for layer-by-layer epitaxial growth on upconverting nanocrystals", *J. Am. Chem. Soc.*, 2012, **134** (27), 11068–11071.

[52] F. Wang, J. Wang, and X. Liu, "Direct evidence of a surface quenching effect on size-dependent luminescence of upconversion nanoparticles", *Angew. Chem., Int. Ed.*, 2010, **49** (41), 7456–7460.

[53] F. Zhang, R. Che, X. Li, C. Yao, J. Yang, D. Shen, P. Hu, W. Li, and D. Zhao, "Direct imaging the upconversion nanocrystal core/shell structure at the subnanometer level: shell thickness dependence in upconverting optical properties", *Nano Let.*, 2012, **12** (6), 2852–2858.

[54] N. A. Kumar, M. A. Dar, R. Gul, and J.-B. Baek, "Graphene and molybdenum disulfide hybrids: synthesis and applications", *Mater. Today*, 2015, **18** (5), 286–298.

[55] J Leclercq and P Sveshtarov, "The Transfer of Graphene: A Review.", *Bul. J. Phy.*, 2016, **43** (2).

[56] L. Liao, H. Peng, and Z. Liu, "Chemistry makes graphene beyond graphene", *J. Am. Chem. Soc.*, 2014, **136** (35), 12194–12200.

[57] F. Giannazzo, S. Sonde, and V. Raineri, "Electronic properties of graphene probed at the nanoscale", *Phys. Appl. Graphene - Exp*, 2011, 353–376.

[58] A. C. Neto, F. Guinea, N. M. Peres, K. S. Novoselov, and A. K. Geim, "The electronic properties of graphene", *Rev. Mod. Phys.*, 2009, **81** (1), 109.

[59] Z. Liu, S.-M. Zhang, J.-R. Yang, J. Z. Liu, Y.-L. Yang, and Q.-S. Zheng, "Interlayer shear strength of single crystalline graphite", *Acta Mec. Sin.*, 2012, **28** (4), 978–982.

[60] K. S. Novoselov, A. K. Geim, S. V. Morozov, D. Jiang, M. I. Katsnelson, I. Grigorieva, S. Dubonos, and a. Firsov, "Two-dimensional gas of massless Dirac fermions in graphene", *Nature*, 2005, **438** (7065), 197–200.

[61] P. V. Pham, "Cleaning of graphene surfaces by low-pressure air plasma", *R. Soc. Open Sci.*, 2018, **5** (5), 172395.

[62] S. Dayou, B. Vigolo, J. Ghanbaja, M. I. Kairi, M. K. N. M. Zuhan, and A. R. Mohamed, "Direct growth of graphene on MgO by chemical vapor deposition for thermal conductivity enhancement of phase change material", *Mat. Chem. Phys.*, 2017, **202**, 352–357.

[63] L. Yan, Y. B. Zheng, F. Zhao, S. Li, X. Gao, B. Xu, P. S. Weiss, and Y. Zhao, "Chemistry and physics of a single atomic layer: strategies and challenges for functionalization of graphene and graphene-based materials", *Chem. Soc. Rev.*, 2012, **41** (1), 97–114.

[64] K. Novoselov and V. Fal, "Ko, L. Colombo, PR Gellert, MG Schwab and K. Kim", *Nature*, 2012, **490** (7419), 192–200.

[65] J. W. Suk, R. D. Piner, J. An, and R. S. Ruoff, "Mechanical properties of monolayer graphene oxide", *ACS Nano*, 2010, **4** (11), 6557–6564.

[66] L. Kantorovich, *Quantum Theory of the Solid State: an Introduction*, vol. 136, Dordrecht, Netherlands: Springer Science & Business Media, 2004.

[67] G. W. Flynn, "Perspective: The dawning of the age of graphene", *J. Chem. Phy.*, 2011, **135** (5), 050901.

[68] L. Ren, X. Qi, Y. Liu, Z. Huang, X. Wei, J. Li, L. Yang, and J. Zhong, "Upconversion-P25-graphene composite as an advanced sunlight driven photocatalytic hybrid material", *J. Mat. Chem.*, 2012, **22** (23), 11765–11771.

[69] M. B. Wabuyele, F. Yan, G. D. Griffin, and T. Vo-Dinh, "Hyperspectral surface-enhanced Raman imaging of labeled silver nanoparticles in single cells", *Rev. Sci. Instrum.*, 2005, **76** (6), 063710.

[70] A. A. Gowen, C. P. O'Donnell, P. J. Cullen, G. Downey, and J. M. Frias, "Hyperspectral imaging–an emerging process analytical tool for food quality and safety control", *Trends Food Sci. Technol.*, 2007, **18** (12), 590–598.

[71] A Yakovliev, R Ziniuk, D Wang, B Xue, L. Vretik, O. Nikolaeva, M Tan, G Chen, Y. L. Slominskii, J Qu, et al., "Hyperspectral multiplexed biological imaging of nanoprobes emitting in the short-wave infrared region", *Nanoscale Res. Let.*, 2019, **14** (1), 1–11.

[72] E. M. Rodrigues and E. Hemmer, "Trends in hyperspectral imaging: from environmental and health sensing to structure-property and nano-bio interaction studies", *Anal. Bio. Chem.*, 2022, **414** (15), 4269–4279.

[73] N. Panov, D. Lu, E. Ortiz-Rivero, E. Martinazzo Rodrigues, P. Haro-González, D. Jaque, and E. Hemmer, "Hyperspectral Imaging and Optical Trapping: Complementary Tools for Assessing Direction-Dependent Polarized Emission from Single Upconverting $LiYF_4$: Yb^{3+}/Er^{3+} Microparticles", *Adv. Opt. Mater.*, 2021, **9** (12), 2100101.

[74] S. Li, W. Song, L. Fang, Y. Chen, P. Ghamisi, and J. A. Benediktsson, "Deep learning for hyperspectral image classification: An overview", *IEEE Trans. Geosci. Rem. Sens.*, 2019, **57** (9), 6690–6709.

[75] X. Dong, M. Jakobi, S. Wang, M. H. Köhler, X. Zhang, and A. W. Koch, "A review of hyperspectral imaging for nanoscale materials research", *Appl. Spectrosc. Rev.*, 2019, **54** (4), 285–305.

[76] K. B. Beć, J. Grabska, G. K. Bonn, M. Popp, and C. W. Huck, "Principles and applications of vibrational spectroscopic imaging in plant science: A review", *Front. Plant Sci.*, 2020, **11**, 1226.

[77] H. Li, X. Wang, T. Y. Ohulchanskyy, and G. Chen, "Lanthanide-doped near-infrared nanoparticles for biophotonics", *Ad. Mat.*, 2021, **33** (6), 2000678.

[78] M. Kataria, K. Yadav, G. Haider, Y. M. Liao, Y.-R. Liou, S.-Y. Cai, H.-i. Lin, Y. H. Chen, C. R. Paul Inbaraj, K. P. Bera, et al., *ACS Photonics*, 2018, **5** (6), 2336–2347.

[79] A. Lay, O. H. Sheppard, C. Siefe, C. A. McLellan, R. D. Mehlenbacher, S. Fischer, M. B. Goodman, and J. A. Dionne, "Optically robust and biocompatible mechanosensitive upconverting nanoparticles", *ACS Cent. Sci.*, 2019, **5** (7), 1211–1222.

[80] S. Wilhelm, M. Kaiser, C. Würth, J. Heiland, C. Carrillo-Carrion, V. Muhr, O. S. Wolfbeis, W. J. Parak, U. Resch-Genger, and T. Hirsch, "Water dispersible upconverting nanoparticles: effects of surface modification on their luminescence and colloidal stability", *Nanoscale*, 2015, **7** (4), 1403–1410.

[81] S. F. Himmelstoß and T. Hirsch, "Long-term colloidal and chemical stability in aqueous media of $NaYF_4$-type upconversion nanoparticles modified by ligand-exchange", *Part. Part. Syst. Charact.*, 2019, **36** (10), 1900235.

[82] M. Lin, Y. Zhao, S. Wang, M. Liu, Z. Duan, Y. Chen, F. Li, F. Xu, and T. Lu, "Recent advances in synthesis and surface modification of lanthanide-doped upconversion nanoparticles for biomedical applications", *Biotech. Adv.*, 2012, **30** (6), 1551–1561.

[83] P. Qiu, N. Zhou, H. Chen, C. Zhang, G. Gao, and D. Cui, "Recent advances in lanthanide-doped upconversion nanomaterials: synthesis, nanostructures and surface modification", *Nanoscale*, 2013, **5** (23), 11512–11525.

[84] L.-P. Ma, W. Ren, and H.-M. Cheng, "Transfer methods of graphene from metal substrates: A review", *Small Methods*, 2019, **3** (7), 1900049.

[85] M. Chen, R. C. Haddon, R. Yan, and E. Bekyarova, "Advances in transferring chemical vapour deposition graphene: a review", *Materials Horizons*, 2017, **4** (6), 1054–1063.

[86] C. Mattevi, H. Kim, and M. Chhowalla, "A review of chemical vapour deposition of graphene on copper", *J. Mater. Chem.*, 2011, **21** (10), 3324–3334.

[87] V. K. LaMer and R. H. Dinegar, "Theory, production and mechanism of formation of monodispersed hydrosols", *J. Am. Chem. Soc.*, 1950, **72** (11), 4847–4854.

[88] T. J. Woehl, C. Park, J. E. Evans, I. Arslan, W. D. Ristenpart, and N. D. Browning, "Direct observation of aggregative nanoparticle growth: Kinetic modeling of the size distribution and growth rate", *Nano Let.*, 2014, **14** (1), 373–378.

[89] N. T. Thanh, N Maclean, and S Mahiddine, "Mechanisms of nucleation and growth of nanoparticles in solution", *Chem. Rev.*, 2014, **114** (15), 7610–7630.

[90] H.-X. Mai, Y.-W. Zhang, R. Si, Z.-G. Yan, L.-d. Sun, L.-P. You, and C.-H. Yan, "High-quality sodium rare-earth fluoride nanocrystals: controlled synthesis and optical properties", *J. Am. Chem. Soc.*, 2006, **128** (19), 6426–6436.

[91] A. Valério and S. L. Morelhao, "Usage of Scherrer's formula in X-ray diffraction analysis of size distribution in systems of monocrystalline nanoparticles", *arXiv preprint arXiv:1911.00701*, 2019,

[92] M Toro-González, D. M. Clifford, R. Copping, S. Mirzadeh, and J. V. Rojas, "Synthesis and characterization of intrinsically radiolabeled lanthanide phosphate nanoparticles toward biomedical and environmental applications", *J. Nanopart. Res.*, 2018, **20**, 1–15.

[93] M. K. Thakur, A. Gupta, S. Ghosh, and S. Chattopadhyay, "Graphene-conjugated upconversion nanoparticles as fluorescence-tuned photothermal nanoheaters for desalination", *ACS Appl. Nano Mater.*, 2019, **2** (4), 2250–2259.

[94] A. Sedlmeier, D. E. Achatz, L. H. Fischer, H. H. Gorris, and O. S. Wolfbeis, "Photon upconverting nanoparticles for luminescent sensing of temperature", *Nanoscale*, 2012, **4** (22), 7090–7096.

[95] S. Sarkar, C. Hazra, and V. Mahalingam, "Scaling down the size of $BaLnF_5$ nanocrystals (Ln= La, Gd, and Lu) with the Ln^{3+} size", *Dalton Trans.*, 2013, **42** (1), 63–66.

[96] X. Cheng, H. Ge, Y. Wei, K. Zhang, W. Su, J. Zhou, L. Yin, Q. Zhan, S. Jing, and L. Huang, "Design for brighter photon upconversion emissions via energy level overlap of lanthanide ions", *ACS Nano*, 2018, **12** (11), 10992–10999.

[97] W. Zhang, H. Jia, H. Ye, T. Dai, X. Yin, J. He, R. Chen, Y. Wang, and X. Pang, "Facile fabrication of transparent and upconversion photoluminescent nanofiber mats with tunable optical properties", *ACS Omega*, 2018, **3** (7), 8220–8225.

[98] H.-X. Mai, Y.-W. Zhang, L.-D. Sun, and C.-H. Yan, "Highly efficient multicolor up-conversion emissions and their mechanisms of monodisperse $NaYF_4$: Yb, Er core and core/shell-structured nanocrystals", *J. Phy. Chem.*, 2007, **111** (37), 13721–13729.